Neural Image Compression: Generalization, Robustness, and Spectral Biases

Kelsey Lieberman

Department of Computer Science
Duke University
Durham, NC USA
kelsey.lieberman@duke.edu

Charles Godfrey

Pacific Northwest National Laboratory Richland, WA USA charles.godfrey@pnnl.gov

James Diffenderfer

Lawrence Livermore National Laboratory Livermore, CA USA diffenderfer2@llnl.gov

Bhavya Kailkhura

Lawrence Livermore National Laboratory Livermore, CA USA kailkhura1@llnl.gov

Abstract

Recent neural image compression (NIC) advances have produced models which are starting to outperform traditional codecs. While this has led to growing excitement about using NIC in real-world applications, the successful adoption of any machine learning system in the wild requires it to generalize (and be robust) to unseen distribution shifts at deployment. Unfortunately, current research lacks comprehensive datasets and informative tools to evaluate and understand NIC performance in real-world settings. To bridge this crucial gap, first, this paper presents a comprehensive benchmark suite to evaluate the out-of-distribution (OOD) performance of image compression methods. Specifically, we provide CLIC-C and Kodak-C by introducing 15 corruptions to popular CLIC and Kodak benchmarks. Next, we propose spectrally inspired inspection tools to gain deeper insight into errors introduced by image compression methods as well as their OOD performance. We then carry out a detailed performance comparison of a classical codec with several NIC variants, revealing intriguing findings that challenge our current understanding of the strengths and limitations of NIC. Finally, we corroborate our empirical findings with theoretical analysis, providing an in-depth view of the OOD performance of NIC and its dependence on the spectral properties of the data. Our benchmarks, spectral inspection tools, and findings provide a crucial bridge to the real-world adoption of NIC. We hope that our work will propel future efforts in designing robust and generalizable NIC methods. Code and data will be made available at https://github.com/klieberman/ood_nic.

1 Introduction

Consider the Mars Exploration Rover, whose scientific objective is to search for clues to past activity of water (and perhaps life) on Mars. To achieve this, the rover collects images of interesting rocks and soils to be analyzed by the scientists on Earth. Sending these images down the Earth-bound data stream in their original form is too slow and expensive due to limited bandwidth. Thus, it is well accepted that image compression could play a key role in producing scientific breakthroughs [41].

Employing image compression in such a setting is challenging for three main reasons: 1) a *high* compression ratio is desired due to low communication bandwidth, 2) given the battery-operated nature of these devices, the compression module has to be *lightweight* so it consumes less memory and

power, and 3) robustness and generalization to environmental noises and domain shifts, respectively, is desired due to limited Mars-specific training data. These requirements are not specific only to the planetary exploration use case but arise in a wide range of scientific applications using image compression in the wild [32].

Recently, neural image compression (NIC) has demonstrated remarkable performance in terms of rate-distortion and runtime overhead on in-distribution (IND) data [9, 42]—satisfying requirements 1) and 2). However, there is limited work on understanding the out-of-distribution (OOD) robustness and generalization performance of image compression methods (requirement 3) [39]. Our work is driven by several open fundamental empirical and theoretical questions around this crucial issue.

How can the expected OOD performance of image compression models be reliably assessed? Can we gain a deeper understanding of the modus operandi of different image compression methods? How do training data properties and biases impact data-driven compression methods?

Main Contributions: This paper takes a critical view of the state of image compression and makes several contributions toward answering the aforementioned questions. • First, we design *compre*hensive benchmark datasets for evaluating the OOD performance of image compression methods. Inspired by existing OOD benchmarks for classification and detection [25, 27, 50, 49], we design CLIC-C and Kodak-C by introducing 15 common shifts emulating train-deployment distribution mismatch to the popular CLIC and Kodak datasets. ② Next, we focus on understanding the image compression performance. The de-facto approach is to use rate-distortion (RD) curves measured with perceptual quality metrics, such as PSNR. Such scalar metrics, although easy to compute, are known to be extremely limited in what they can capture and sometimes can even be misleading [55, 53]. To complement RD curves, we propose spectrally-inspired inspection tools that provide a more nuanced picture of (a) compression error, and (b) OOD performance of a given method. Specifically, we introduce a power spectral density (PSD) based approach to understand the reconstruction error. Our approach not only quantifies how much error was made but also highlights precisely where it was made (in the frequency domain). Similarly, to understand the OOD performance of a compression method in unseen deployment scenarios, we propose Fourier error heatmaps—a visualization tool for highlighting the sensitivity of the reconstruction performance of a compression method to different perturbations in the frequency domain. **3** Using our benchmark datasets and inspection tools, we carry out a systematic empirical comparison of classical codecs (i.e., JPEG2000, VTM) with various variants of NIC models (e.g., original, variable rate, pruned). • Finally, we develop theoretical tools to connect NIC OOD performance with its training data properties.

Main Findings: Our analysis resulted in some invaluable insights about the state of image compression. We summarize some of our findings below.

- NIC produces inherently different spectral artifacts than classical codecs even when both methods have the same PSNR (or compression rate) in many cases. Our tools help uncover this hidden spectral bias and highlight the limitations of de-facto RD curve-based performance comparison.
- As the compression rate increases, NIC and classical codecs prioritize encoding different frequencies, in turn, highlighting that they use very different compression mechanisms. By precisely characterizing this behavior, our tools help in advancing the current understanding of the modus operandi of image compression methods.
- In OOD settings, NIC and classical codecs can fail (or succeed) in the same (or different) ways.
 By attributing the successful and failed cases to the spectral characterization of OOD shifts in our
 benchmark dataset, we gain a holistic understanding of the OOD performance of image compression
 methods.
- Identifying the suitable compression method becomes exceptionally challenging without the knowledge of spectral characteristics of OOD shifts. Our systematic evaluation identifies this open issue with current compression methods and suggests the design of next-generation NIC models that can adapt themselves at runtime based on the spectral nature of the data to be a potentially worthwhile direction to pursue in the future.

We corroborate our findings with a detailed theoretical analysis, showing that multiple overarching trends in our experimental results can be attributed to neural compression models' spectral bias.

Appendix A has a detailed related work discussion, while all references are listed in the main paper.

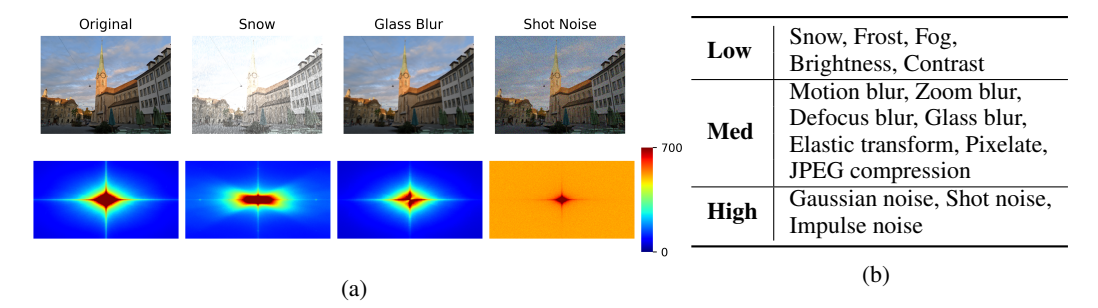


Figure 1: (a) **Top row:** An original CLIC image and the same image with 3 different corruptions in CLIC-C (severity 5). **Bottom left:** Average PSD of CLIC dataset, $\frac{1}{N}\sum_{k=1}^{N}PSD(X_k)$. **Bottom row, other figures:** Average PSD of the difference between the corrupted images and the clean images for each given CLIC-C corruption c, $\frac{1}{N}\sum_{k=1}^{N}PSD(c(X_k)-X_k)$. (b) CLIC-C corruptions categorized as low, medium, or high based on corruption average PSD.

2 Out-of-distribution image compression datasets

To evaluate NIC in the presence of environmental or digital distribution shifts, we generated variants of the CLIC and Kodak datasets, which we refer to as CLIC-C and Kodak-C. Following the techniques presented in [25] for studying the performance of DNN classifiers encountering distributional shifts "in the wild", our -C datasets consist of images augmented by 15 common corruptions. For each image in the original dataset, the -C dataset contains a corrupted version of the image for each of the 15 common corruptions¹, and for each of five corruption severity levels, with 1 being the lowest severity and 5 being the highest. A sample of some corruptions on CLIC-C is provided in Figure 1a.

While each -C dataset offers a broad sampling of environmental or digital image corruptions, it also provides a spectrally diverse collection of corruptions, in the sense that each corruption can be categorized as low, medium, or high frequency based on the frequency content used for perturbations. We will write $PSD(\cdot)$ to denote the function that converts the input image from the spatial to the frequency domain by computing the power spectral density of the input. Practically, computing $PSD(\cdot)$ is done by applying the fast Fourier transform (FFT) [11], followed by a shift operation to center the zero-frequency component, then taking the absolute value. Now suppose we have a set $\mathcal{X} = \{X_k\}_{k=1}^N$ of uncorrupted images and some corruption function $c(\cdot)$ (e.g., frost, gaussian noise, etc.). We analyze the spectrum each corruption $c(\cdot)$ by computing $\frac{1}{N}\sum_{i=1}^N PSD(X_i-c(X_i))$ (see Figure 1a). Identifying the dominant frequencies in the Fourier spectrum for each corruption yields a rough categorization into low, medium, and high-frequency corruptions, provided in Table 1b.

3 Spectral inspection tools

While existing scalar metrics, such as PSNR, are able to summarize the visual similarity of reconstructed images to the original, we will demonstrate that such metrics can provide an incomplete (and sometimes misleading) picture when measuring the impact of compression in OOD settings. Notably, existing tools do not consider the impact of compression on different frequency ranges of images within a dataset. To more thoroughly analyze the effects of image compression, we propose to measure and visualize the effect of image compression in the spectral domain. Given an image compression model \mathcal{C} that returns reconstructed images, we introduce tools for analyzing compression error in the Fourier domain to better understand (i) which spectral frequencies are distorted by \mathcal{C} , (ii) the OOD generalization error, and (iii) the robustness error in the presence of distributional shifts.

Definition 3.1 (Spectral Measure of Distortion Error). To analyze (i), we evaluate the image compression model \mathcal{C} 's ability to reconstruct components of an image across a range of frequencies. To quantify this, we compute the average PSD of the difference between each image X_k in a dataset \mathcal{X} and the reconstructed version $\mathcal{C}(X_k)$ of X_k : $\mathcal{D}(\mathcal{C},\mathcal{X}):=\frac{1}{N}\sum_{k=1}^N PSD(X_k-\mathcal{C}(X_k))$.

¹We used github.com/bethgelab/imagecorruptions to apply corruptions to Kodak and CLIC images

Definition 3.2 (Spectral Measure of OOD Generalization Error). For (ii), we evaluate \mathcal{C} 's ability to faithfully reconstruct OOD images. To quantify this, we extend the metric $\mathcal{D}(\mathcal{C},\mathcal{X})$ to account for a corrupted version $c(\mathcal{X})$ of \mathcal{X} as follows: $\mathcal{G}(\mathcal{C},\mathcal{X},c):=\frac{1}{N}\sum_{k=1}^{N}PSD(c(X_k)-\mathcal{C}(c(X_k)))$.

Definition 3.3 (Spectral Measure of OOD Robustness Error). For (iii), we evaluate \mathcal{C} 's denoising ability. To quantify this, we compute the average PSD of the difference between each uncorrupted image X_k and the reconstructed version $\mathcal{C}(c(X_k))$ of the corresponding corrupted image $c(X_k)$: $\mathcal{R}(\mathcal{C},\mathcal{X},c):=\frac{1}{N}\sum_{k=1}^{N}PSD(X_k-\mathcal{C}(c(X_k)))$.

For simplicity, when (C, \mathcal{X}, c) is clear from the context, we will just write D, G, or R. Note that G provides insight into the compression model C's ability to generalize to a distribution shift C while R visualizes the denoising effect (or lack thereof) of C across the frequency domain.

In Appendix B, we present results using an additional tool, *the Fourier heatmap*, that utilizes Fourier basis perturbations as corruptions and is used to corroborate our findings for the specific -C datasets and corruptions we consider. This tool can be leveraged when specific OOD data is unavailable.

4 Experiments and findings

We analyze the performance of the following image compression methods. Further details on their model architectures and training can be found in Appendices I to L.

Classical codecs: We apply the JPEG2000 algorithm over several compression rates q.

Neural Image Compressors (NIC): NIC model optimization uses a hyperparameter λ to control the relative weight of distortion (quality of reconstruction) and rate (level of compression) terms in the objective function. Our experiments include eight **Fixed-Rate** (**FR**) models, each trained on a single λ value, and one **Variable-Rate** (**VR**) model, trained over a continuous range of λ values using loss conditional training [17]. We include the VR model for two reasons: (a) VR models are more desirable in the wild due to reduced space constraints and (b) to observe how approximating a fixed-rate model as a variable-rate model impacts spectral artifacts across frequencies. For both fixed-and variable-rate the distortion objective is a mean squared error (MSE) (*i.e.*, model is optimized for PSNR), and in both cases, our base NIC architecture is the scale hyperprior model of [9].

All NIC models were optimized on the train split of the 2020 CLIC dataset [52]. Further training details can be found in Appendix L. For NIC, we also (a) designed and analyzed pruned variants, and (b) analyzed MS-SSIM optimized versions. These additional comparisons, as well as comparisons using the additional codec VTM (h.266) [29], are provided in Appendices C and E.

Evaluation setup. We compare distortion, robustness, and generalization error of different image compression methods under three constraints: (a) no constraint, (b) fixed-bpp, and (c) fixed-PSNR. In (a), we compare methods over their full range of rate-distortion tradeoffs by generating rate-distortion curves. In (b), we compare models with hyper-parameters which give a very similar bpp result on a particular dataset. For example, we find that on the CLIC dataset, FR NIC with $\lambda=0.15$, VR NIC with $\lambda=0.21$, and JPEG2000 with q=10, all give a bpp very close to 1.21. Thus, comparing these three models with those hyper-parameters on CLIC under a fixed bpp constraint, emulates a setting in which a fixed budget is available to store images. Analogously, in (c) we compare models with hyper-parameters yielding a fixed PSNR. This emulates a setting with a requirement on minimum allowable reconstructed image quality. Scenarios (b) and (c) are used when evaluating \mathcal{D} , \mathcal{G} , \mathcal{R} , Fourier heatmaps, and accuracy on a downstream task.

Test data. All models are tested on (a) in-distribution (IND) and (b) corrupted (or OOD) datasets. For (a), we use the 2020 CLIC test split, the full Kodak dataset, and the ImageNet validation split. For (b), we use the corresponding -C datasets for each of the datasets in (a). The main body contains results for the CLIC/CLIC-C dataset. Analogous results for Kodak are in Appendix F.

4.1 Evaluating spectral distortion on IND data

On in-distribution (IND) data, the existing RD curve metrics in the center of Figure 2 highlight the established trend that NIC models outperform the JPEG2000 model over the compression rates that the NIC model is trained on (bpp $\in (0.1, 1.5)$) [9]. VR NIC obtains the same performance as FR NIC for low and moderate bpps; however, the FR NIC model outperforms the VR NIC model at higher

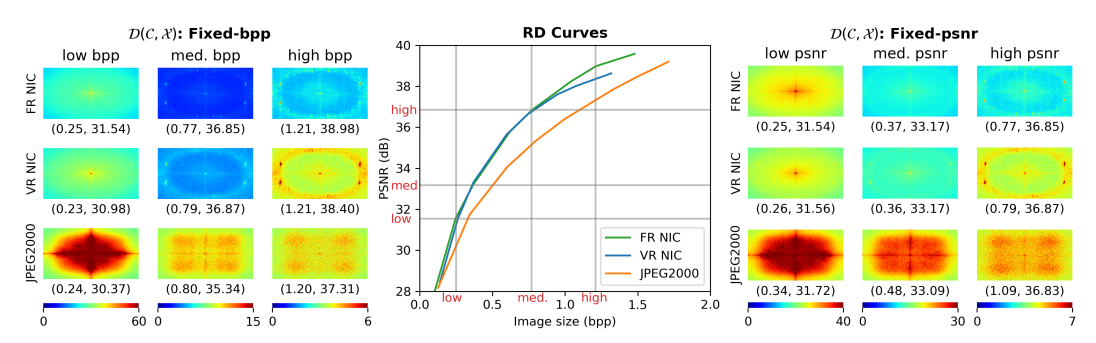


Figure 2: **Visualizing distortion via CLIC test set evaluation. Left:** spectral measure of indistribution reconstruction error \mathcal{D} under the fixed-bpp constraint at three rates. **Center:** Rate-distortion curves with vertical lines indicating fixed-bpp values and horizontal lines indicating fixed-PSNR values. **Right:** \mathcal{D} under fixed-PSNR constraint. Each \mathcal{D} plot is labeled with a tuple of that model's (bpp, PSNR) on CLIC. Hotter colors (red) indicate more error in that frequency range.

bpps, despite the fact that both models were trained on the same range of λ . This result follows [17] and suggests that the VR NIC may not be expressive enough to learn the high PSNR regime.

Next, we use our spectral inspection tool \mathcal{D} to better understand the effects of different image compression methods. Specifically, Figure 2 shows plots of \mathcal{D} under three fixed-bpp and three fixed-PSNR scenarios on the clean CLIC dataset. We highlight some surprising insights below.

Two methods yielding the same PSNR (or bpp) can produce very different spectral artifacts. Under the fixed-PSNR constraint (right side of Figure 2), each column consists of methods with hyper-parameters selected to give very similar PSNRs on the CLIC test set (e.g., models on the "high psnr" column all have PSNR ≈ 36.85). Despite having comparable PSNRs, the plots of $\mathcal D$ vary greatly between the NIC models and JPEG2000. In particular, NIC models distort high frequencies significantly more than medium frequencies (notice the warmer-colored rings around the edges of the $\mathcal D$ plots with cooler-colored centers). JPEG2000, on the other hand, distorts low and medium frequencies more than high frequencies (notice the large rectangles of warmer colors). This same pattern holds under the fixed-bpp constraint (left side of Figure 2). Furthermore, VR NIC and FR NIC have the same error patterns, but VR NIC does leave a slightly higher magnitude of error in some settings (e.g., med. bpp, high bpp, and high psnr). This suggests that NIC models produce inherently different spectral artifacts than classical codecs.

As the compression rate increases, NIC and JPEG2000 prioritize different parts of the spectrum. On the left side of Figure 2, each column represents a different "budget" scenario where the three methods have hyper-parameters which result in the models giving very similar bpps on the CLIC test set. Although it was previously known that the quality of the reconstructed images decreases as the bpp decreases, it was not previously known *which* frequencies NIC models distort to achieve a given bpp. The \mathcal{D} plots show that JPEG2000 models corrupt low- and mid-frequency regions starting at low and moderate compression rates and these regions become more severe as the budget decreases. NIC models do almost the opposite—they sacrifice the highest frequencies first and expand this region into lower frequencies at more severe compression rates (*i.e.*, as bpp decreases). These observations demonstrate that *NICs use a very different compression mechanism than classical codecs*.

4.2 Evaluating the generalization and the robustness on OOD data

We use the CLIC-C dataset and our spectral tools to study the OOD performance of different image compression methods. We show results for example shifts (one low, medium, and high-frequency representative) and three severities (1, 3, and 5 where 5 is most severe) in Figures 3 and 4 and discuss several interesting findings below. Remaining results are reported in Appendices C, E, and H.

4.2.1 Rate-distortion curves on OOD data

Image compression models generalize to low- and mid-frequency shifts better than high-frequency shifts. The top row of Figure 3 shows how well different compression models generalize to shifted images in terms of RD curves. In other words, these plots show how well a compressor \mathcal{C} can

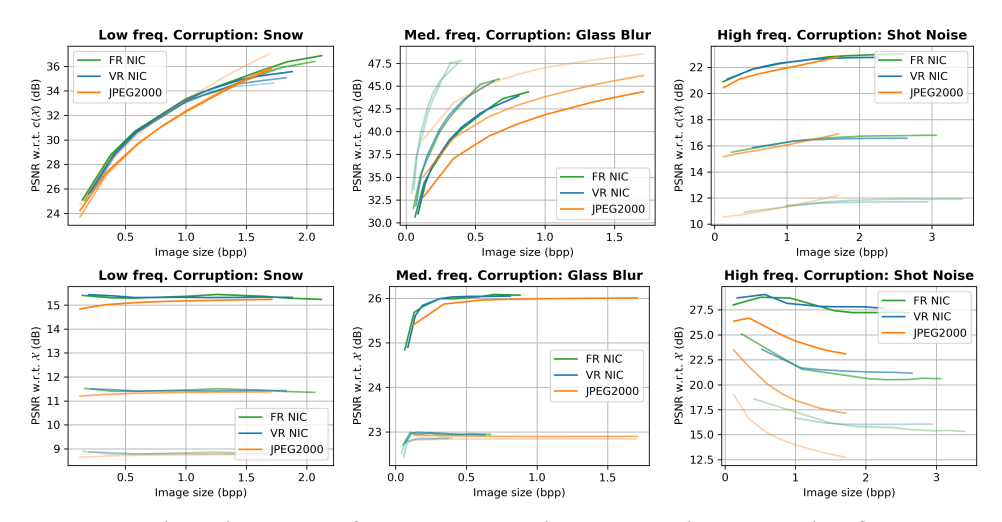


Figure 3: Rate-distortion curves for a representative low, medium, and high-frequency shift. Each shift and model has three curves for severity=1 (least transparent), severity=3, and severity=5 (most transparent). Top row: generalization of $\mathcal{C}(c(\mathcal{X}))$ w.r.t. $c(\mathcal{X})$ (i.e., PSNR of the reconstructed shifted images w.r.t. the original shifted images). Bottom row: denoising of $\mathcal{C}(c(\mathcal{X}))$ w.r.t. \mathcal{X} (i.e., PSNR of the reconstructed shifted images w.r.t. the original clean images).

reconstruct a given shifted image $c(\mathcal{X})$ in terms of PSNR of $\mathcal{C}(c(\mathcal{X}))$ with respect to $c(\mathcal{X})$. The three examples of corruption in this figure show vastly different trends. On the low-frequency corruption (snow), all three models can reconstruct $c(\mathcal{X})$ almost as well as these models can reconstruct clean images (note the PSNR range in the top left plot of Figure 3 is about 24-37 while the PSNR range for the clean data in Figure 2 is about 28-40). Interestingly, the three models can reconstruct the images with the glass blur (a medium-frequency shift) better than they can reconstruct clean images (the PSNR of the data shifted with glass blur ranges from about 31-48). These results suggest that image compression models are fairly effective at generalizing to low-frequency shifts and very effective at generalizing to medium-frequency shifts. However, the high-frequency shift (shot noise), gives a starkly different result. All three models give very low PSNRs with respect to $c(\mathcal{X})$. Even at the lowest severity (severity=1), this PSNR is only in the low 20s. As the severity increases (i.e., as the lines become more transparent), the PSNR decreases even more to the point that, at the highest severity, none of the models can achieve a PSNR higher than 12.5. Notably, the main factor determining the PSNR is the severity of the corruption and not model type or bpp. This suggests that it is significantly harder to generalize to high-frequency data than to low- or mid-frequency data.

NIC models' bpp usage is highly sensitive to the data shift type. In the previous point, we saw that, for each corruption, all three models achieved very similar PSNRs with respect to $c(\mathcal{X})$. The RD curves for these models, however, differ significantly because these models use different bpps to achieve these PSNRs². In general, JPEG2000 is very consistent in terms of its bpp usage—it uses 0-2 bpps regardless of the corruption type. NIC models, however, give different bpp ranges depending on the frequency of the shift. In particular, NIC models require fewer bpps to reconstruct the glass blur shifted images (e.g., both NIC models and JPEG2000 can achieve PSNRs with respect to $c(\mathcal{X})$ of > 45; however, the NIC models need bpp < 1, while JPEG2000 needs bpp > 1.5). This suggests that NIC models can capitalize on "easier to model" images. On the other hand, NIC models may also increase the bpp to no avail. Consider the shot noise corruption (a high-frequency corruption): here NIC models use much higher bpps (up to bpp=4). Despite this significant increase in bpp, the NIC models are unable to increase the PNSR (notice how the curves are almost flat). This highlights that although NIC and JPEG2000 can achieve similar PSNRs on a given shift, NIC is significantly more sensitive to the shift type than JPEG2000 in terms of the compression rate required to achieve these PSNRs.

NIC models are better at denoising high-frequency corruptions than JPEG2000. The second row of Figure 3 shows how well different compressors C denoise corrupted images in terms of

²Note that we use the same values for λ on NIC models and quality q on JPEG2000 for the corruptions as we do for the clean images.

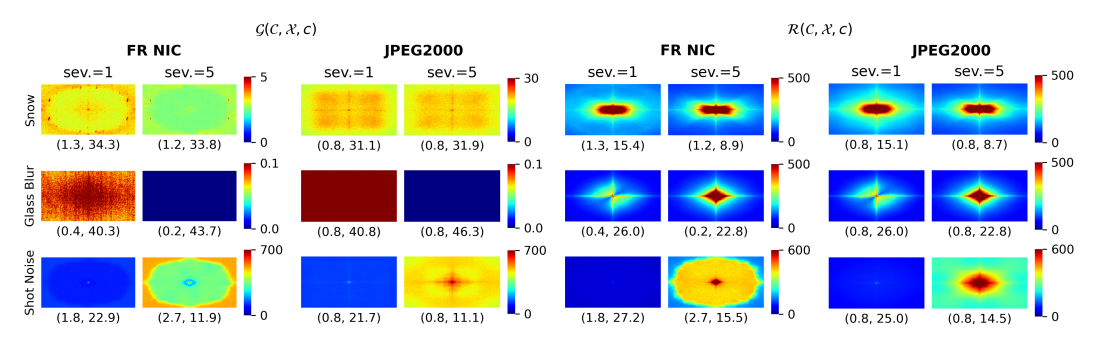


Figure 4: Generalization error \mathcal{G} and denoising error \mathcal{R} for FR NIC and JPEG2000. We plot both spectral metrics for one low, medium, and high-frequency corruption at severities 1 and 5. Each plot is labeled with a tuple of that model's (bpp, PSNR) on the CLIC-C dataset with that corruption.

the PSNR of $C(c(\mathcal{X}))$ with respect to \mathcal{X} . These results show that all the models fail at denoising snow (low-frequency) and glass blur (medium-frequency) corruptions (PSNR does not change much with an increase in bpp). However, NIC and JPEG2000 show different performances in terms of denoising high-frequency corruptions. Specifically, NIC models achieve significantly better PSNR with respect to \mathcal{X} than JPEG2000. This suggests that NICs may be a more effective method for denoising high-frequency corruptions than the previously-used JPEG and JPEG2000 methods. The implication of this finding extends to the research area of adversarial example denoising [5].

4.2.2 Spectral analysis on OOD data

We now take a deeper look at the Section 4.2.1 findings using our spectral inspection tools. We report only FR NIC results here as VR NIC results are very similar (see Figure 10 in Appendix D).

Spectral artifacts are similar for low-frequency shifts and clean images. The patterns of $\mathcal G$ in Figure 4 measure how well each model generalizes to (or reconstructs) the shifted images. For the low-frequency shift (Figure 4 left side, top row), the four plots look strikingly similar to the patterns exhibited by the same models on clean data (Figure 2 top and bottom row): NIC models distort high frequencies more than low frequencies while JPEG2000 distorts low and medium frequencies more than high frequencies. This suggests that both methods' modus operandi for generalization to data with low-frequency shifts is similar to their modus operandi on clean data, which makes sense as clean data is dominated by low/mid frequencies. Interestingly, these generalization differences between NIC and JPEG2000 compressors are not accompanied by differences in $\mathcal R$. Both methods show similar patterns in their plots of $\mathcal R$ patterns and these in turn look similar to the snow corruption plot in Figure 1a. This is consistent with our finding from Figure 3 which showed that both NIC and JPEG2000 fail to denoise low-frequency corruptions. In other words, Figure 4 shows that NIC and JPEG2000 fail in a very similar manner on low-frequency signal denoising tasks.

NIC and JPEG2000 make almost no generalization error on medium-frequency shifts. The left side of the second row of Figure 4 shows that both FR NIC and JPEG2000 have very small generalization errors (magnitudes < 0.2), and this low error is relatively uniform across all frequencies. This shows that both models are very effective at reconstructing all the frequencies in images with glass blur—in fact, they can reconstruct these images better than they can reconstruct clean images—corroborating our first finding in Section 4.2.1. Again the $\mathcal R$ plots for glass blur for both of these models look very similar to Figure 1a; this similarity has a simple explanation due to a fundamental tradeoff between generalization and robustness. This relationship between $\mathcal R$, $\mathcal G$ and average PSD of corruptions is described more precisely in Appendix M.4.

High-frequency corruptions exaggerate differences observed in spectral artifacts between NIC and JPEG2000 on clean data. Section 4.2.1 highlighted that high-frequency signals severely degrade the generalization performance of all image compression methods. From the RD curves with respect to the corrupt images (top right plot in Figure 3), we observe that at each severity the three models have almost identical performance in the usual 0-2 bpp range. These results might lead us to expect that these models make similar reconstruction mistakes, but our spectral inspection tools indicate that this is not the case at all. Our plots of \mathcal{G} on shot noise at severity=5 (bottom row, columns 2 and 4 of Figure 4) indicate that NIC models distort the higher frequencies significantly more than

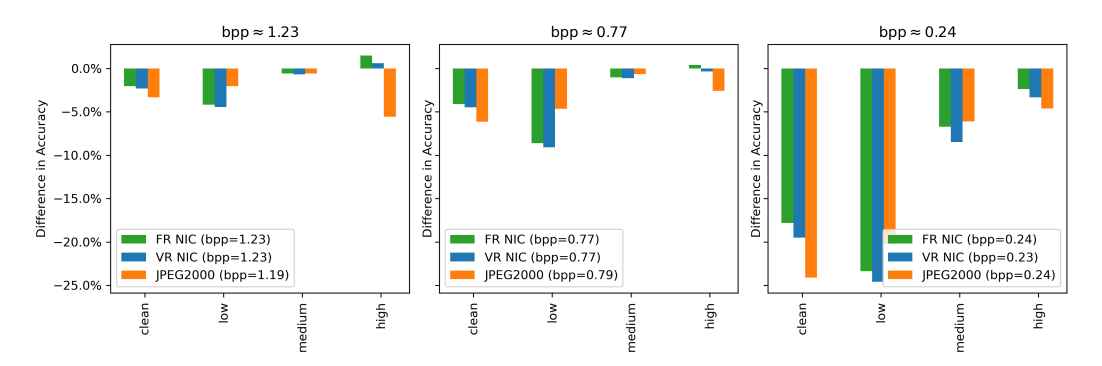


Figure 5: Effect of compressing corrupt images on classification accuracy. Each bar shows the average difference in accuracy after compressing with different methods $\mathcal C$ for a group of corruptions as classified in Table 1b. Specifically, let A(X) be the top-1 accuracy of the model on dataset X, measured in percentage points. Then we report $A(\mathcal C(c(X))) - A(c(X))$ over all -C corruptions in the corruption category (or on clean ImageNet in the case of "clean"). Each subplot shows results under a different fixed-bpp constraint based on the bpps achieved by the compressors on the clean ImageNet dataset. Results for individual corruptions and additional NIC variants are in Appendix C.

the low and medium frequencies while JPEG2000 distorts medium and low frequencies more than high frequencies. Additionally, the bottom right plot of Figure 3 shows that for shot noise, NIC models achieve higher PSNR of the reconstructed corrupt images with respect to the clean images than JPEG2000, i.e. they have a stronger denoising effect. In the bottom right of Figure 4 we see a more detailed picture: for high severity shot noise, NIC models achieve lower $\mathcal R$ in high frequencies. Also, note that the NIC models have the smallest errors in $\mathcal G$ whereas they have the largest errors in $\mathcal R$ and vice versa. Thus, these findings suggest that NIC models behave similarly to a low-pass filter.

4.3 Impact of spectral artifacts on downstream applications

In practice, image compression algorithms may be used as a pre-processing step before images are used for another downstream task. For this reason, practitioners should consider the performance on downstream tasks when comparing compression methods. We analyze the effectiveness of the compression methods on the downstream task of ImageNet classification using a pre-trained ResNet-50 model and report the difference in top-1 accuracy after compression (Figure 5) [24].

NIC can improve the robustness of downstream classification to high-frequency corruptions. However, JPEG2000 is more effective than NIC for low-frequency corruptions. While in general, compression degrades classification performance on clean images (all compressors show negative differences for the "clean" category in Figure 5), one interesting finding is that applying NIC compression at low compression rates can actually improve the robustness of the classification model against high-frequency corruptions. Specifically, at bpp=1.23, the difference in accuracy is positive for high-frequency corruptions with NIC, meaning that the classification model gave a higher accuracy on the set of corrupted images after compression than it did on the original corrupted images. Compressing with JPEG2000 at the same rate caused a degradation in accuracy on these corruptions. However, JPEG2000 has a smaller degradation in accuracy compared to NIC on low-frequency corruptions. Thus, the ideal compressor for downstream tasks is dependent on the type of corruption.

Pruning NIC models amplifies the robustness gains of NIC for downstream classification tasks. Additional experimental results in Appendix C (Figure 9), show that *pruned VR NIC and NIC optimized for MS-SSIM act as even better high-frequency signal denoisers for this application.*

5 Theoretical analysis of the OOD performance of NIC

In this section, we corroborate our empirical findings in the previous section with theoretical results. For simplicity, here we summarize our results on linear autoencoder-based NIC methods. For complete definitions, additional references, and proofs of the following statements, please refer to Appendix M. In Appendix M.3, we also provide a more general result applicable to nonlinear models.

Recall a classical observation: in the setting of linearly auto-encoding a mean-centered distribution, the reconstruction function (*i.e.*, encoder-decoder composition) is a projection onto the high-variance principal components of the input data [18] (see also [6]). Combining this with well-known facts about statistics of natural images, we show that a linear autoencoder applied to a natural image dataset retains only low/mid (spatial) frequency components, which account for the majority of the variance. Using this result, we state theoretical explanations for multiple trends in our experiments³.

Lemma 5.1. Let \mathcal{X} be a dataset of natural images and let $\hat{\mathcal{X}}$ denote its (spatial) discrete Fourier transform. Assume the following (for supporting evidence see Appendix M):

- (I) The principal components of $\hat{\mathcal{X}}$ are roughly aligned with the spatial Fourier frequency basis.
- (II) The associated variances are monotonically decreasing with frequency magnitude (more specifically according to the power law $\frac{1}{|i|^{\alpha}+|j|^{\beta}}$).

If C is a linear autoencoder trained by minimizing MSE on X, with latent space of dimension r, and if " $\tilde{}$ " denotes the spatial discrete Fourier transform, for any data point X with Fourier transform \hat{X}

$$\widehat{\mathcal{C}(X)} pprox egin{cases} \hat{X}_{:,ij} & : i^2 + j^2 \leq rac{r}{\pi K} \ 0 & : otherwise. \end{cases}$$

where K is the number of channels in the images in \mathcal{X} and where $\hat{X}_{:,ij}$ denotes the components of \hat{X} corresponding to spatial frequency (i,j).

Corollary 5.2. Under the hypotheses of Lemma 5.1, the robustness error of C to a corruption c (as defined in Definition 3.3), measured in spatial frequency (i, j), is

$$\mathcal{R}(\mathcal{C}, \mathcal{X}, c)_{ij} \approx \begin{cases} \frac{1}{N} \sum_{k} |\widehat{c(X_k)} - \hat{X_k})_{:,ij}| & : i^2 + j^2 \leq \frac{r}{\pi K} \\ \frac{1}{N} \sum_{k} |\hat{X_k}_{:,ij}| & : otherwise. \end{cases}$$

Corollary 5.3. *Under the hypotheses of Lemma 5.1, the* generalization error of C to a corruption c (as defined in Definition 3.2), measured in spatial frequency (i, j), is

$$\mathcal{G}(\mathcal{C},\mathcal{X},c)_{ij} \approx \begin{cases} 0 & : i^2+j^2 \leq \frac{r}{\pi K} \\ \frac{1}{N} \sum_k \sqrt{|\hat{X}_{:,ij}|^2 + 2\hat{X}_{:,ij}(\widehat{c(X)} - \hat{X})_{:,ij} + |\widehat{(c(X)} - \hat{X})_{:,ij}|^2} & : otherwise. \end{cases}$$

Lemma 5.1 suggests that autoencoder compressors trained on natural images behave like a low-pass filter, in turn, corroborating our claim in Section 4.2.2.

Corollary 5.2 suggests that autoencoder compressors trained on natural images are less robust to corruptions with large amplitude in low frequencies (in the sense that $|(c(X) - X)_{:,ij}|^2$ is large for small values of ij). This is indeed what we see in Figure 3 (bottom left), where snow corruptions are detrimental to PSNR of $\mathcal{C}(c(\mathcal{X}))$ w.r.t. \mathcal{X} , and Figure 4, where the $\mathcal{R}(\mathcal{C},\mathcal{X},c)$ error for the NIC is concentrated in low frequencies. We also observe in Figure 5 that NIC is more beneficial for downstream classification accuracy in the case of high-frequency corruptions (e.g. shot noise) and less beneficial in the case of low-frequency corruptions (e.g. snow).

On the other hand, the conclusion of Corollary 5.3 is more involved than that of Corollary 5.2–the "cross term" $2\hat{X}_{:,ij}(c(X)-\hat{X})_{:,ij}$ is in general non-zero. However, there are many cases where at least an expectation over the data set \mathcal{X} this cross term vanishes (e.g., when c is additive noise). In such cases, Corollary 5.3 suggests that compressor trained on natural images generalize less successfully to shifts with large amplitude in high frequencies. In Figure 3 (top right) we see that shot noise corruptions are detrimental to PSNR of $\mathcal{C}(c(\mathcal{X}))$ w.r.t. $c(\mathcal{X})$, and in Figure 4 we see that for the snow and shot noise corruptions, $\mathcal{G}(\mathcal{C},\mathcal{X},c)$ are in fact concentrated in high frequencies. In summary, with both the theoretical analysis of a simple mathematical model and empirical results, we find that NICs have a strong spectral bias that causes them to overfit to low-frequency training data.

³Since this simplified model has no compression rate objective, one should only expect the above theoretical results to be predictive (or explanatory) of the high bpp/PSNR cases of our experiments.

⁴Moreover glass blur can be viewed as a sort of convolution operator, for which one can verify that the aforementioned cross term is non-zero.

6 Conclusion and future directions

We proposed benchmark datasets and inspection tools to gain a deeper understanding of the robustness and the generalization behavior of image compression models in the wild. Using our spectral inspection tools, we uncovered the modus operandi of different compression methods. We also highlighted similarities and differences among them via a systematic OOD evaluation. While we have taken some first steps to understand the state of existing image compression schemes, many questions remain to be answered. First, exploring the use of our tools in applications beyond image compression is expected to provide interesting insights. Next, designing practical training approaches to overcome brittleness issues is a potentially worthwhile research direction. Finally, developing NIC methods to efficiently adapt to distribution shifts at runtime will mitigate some of these issues.

Acknowledgements

This work was performed under the auspices of the U.S. Department of Energy by Lawrence Livermore National Laboratory under Contract DE-AC52-07NA27344 and was supported by the LLNL-LDRD Program under Project No. 22-DR-009 (LLNL-JRNL-851532).

The third author was supported by the Laboratory Directed Research and Development Program at Pacific Northwest National Laboratory, a multiprogram national laboratory operated by Battelle for the U.S. Department of Energy.

We thank Eleanor Byler for helpful comments on an earlier draft.

References

- [1] Origins of scaling in natural images. *Vision Research*, 37(23):3385–3398, Dec. 1997. ISSN 0042-6989. doi: 10.1016/S0042-6989(97)00008-4.
- [2] Oodhdr-codec: Out-of-distribution generalization for hdr image compression. 36:158-166, Jun. 2022. doi: 10.1609/aaai.v36i1.19890. URL https://ojs.aaai.org/index.php/AAAI/article/view/19890.
- [3] G. Alain and Y. Bengio. What Regularized Auto-Encoders Learn from the Data-Generating Distribution. *Journal of Machine Learning Research*, 15(110):3743–3773, 2014. ISSN 1533-7928.
- [4] J. An and S. Cho. Variational Autoencoder based Anomaly Detection using Reconstruction Probability. 2015.
- [5] A. E. Aydemir, A. Temizel, and T. T. Temizel. The effects of jpeg and jpeg2000 compression on attacks using adversarial examples. *arXiv preprint arXiv:1803.10418*, 2018.
- [6] P. Baldi and K. Hornik. Neural networks and principal component analysis: Learning from examples without local minima. *Neural Networks*, 2(1):53–58, Jan. 1989. ISSN 0893-6080. doi: 10.1016/0893-6080(89)90014-2.
- [7] J. Ballé, V. Laparra, and E. P. Simoncelli. Density modeling of images using a generalized normalization transformation. Nov. 2015.
- [8] J. Ballé, V. Laparra, and E. P. Simoncelli. End-to-end optimized image compression. In International Conference on Learning Representations, 2017. URL https://openreview. net/forum?id=rJxdQ3jeg.
- [9] J. Ballé, D. Minnen, S. Singh, S. J. Hwang, and N. Johnston. Variational image compression with a scale hyperprior. In *International Conference on Learning Representations*, 2018. URL https://openreview.net/forum?id=rkcQFMZRb.
- [10] J. Bégaint, F. Racapé, S. Feltman, and A. Pushparaja. Compressai: a pytorch library and evaluation platform for end-to-end compression research. arXiv preprint arXiv:2011.03029, 2020.

- [11] E. O. Brigham and R. E. Morrow. The fast fourier transform. *IEEE Spectrum*, 4(12):63–70, 1967. doi: 10.1109/MSPEC.1967.5217220.
- [12] G. J. Burton and I. R. Moorhead. Color and spatial structure in natural scenes. *Applied Optics*, 26(1):157–170, Jan. 1987. ISSN 2155-3165. doi: 10.1364/AO.26.000157.
- [13] Y. Choi, M. El-Khamy, and J. Lee. Variable rate deep image compression with a conditional autoencoder. 2019 IEEE/CVF International Conference on Computer Vision (ICCV), pages 3146–3154, 2019.
- [14] F. Croce, M. Andriushchenko, V. Sehwag, E. Debenedetti, N. Flammarion, M. Chiang, P. Mittal, and M. Hein. Robustbench: a standardized adversarial robustness benchmark. In *Thirty-fifth Conference on Neural Information Processing Systems Datasets and Benchmarks Track (Round 2)*, 2021. URL https://openreview.net/forum?id=SSKZPJCt7B.
- [15] J. Diffenderfer and B. Kailkhura. Multi-prize lottery ticket hypothesis: Finding accurate binary neural networks by pruning a randomly weighted network. In *International Conference on Learning Representations*, 2021. URL https://openreview.net/forum?id=U_mat0b9iv.
- [16] J. Diffenderfer, B. R. Bartoldson, S. Chaganti, J. Zhang, and B. Kailkhura. A winning hand: Compressing deep networks can improve out-of-distribution robustness. In A. Beygelzimer, Y. Dauphin, P. Liang, and J. W. Vaughan, editors, *Advances in Neural Information Processing Systems*, 2021. URL https://openreview.net/forum?id=YygAOyppTR.
- [17] A. Dosovitskiy and J. Djolonga. You only train once: Loss-conditional training of deep networks. In *International Conference on Learning Representations*, 2020. URL https://openreview.net/forum?id=HyxY6JHKwr.
- [18] C. Eckart and G. Young. The approximation of one matrix by another of lower rank. *Psychometrika*, 1(3):211–218, Sept. 1936. ISSN 1860-0980. doi: 10.1007/BF02288367.
- [19] J. Frankle and M. Carbin. The lottery ticket hypothesis: Finding sparse, trainable neural networks. 2018. doi: 10.48550/ARXIV.1803.03635. URL https://arxiv.org/abs/1803. 03635.
- [20] J. Frankle, G. K. Dziugaite, D. M. Roy, and M. Carbin. Linear mode connectivity and the lottery ticket hypothesis. In *Proceedings of the 37th International Conference on Machine Learning*, ICML'20. JMLR.org, 2020.
- [21] C. Gille, F. Guyard, M. Antonini, and M. Barlaud. Learning sparse auto-encoders for green ai image coding, 2022. URL https://arxiv.org/abs/2209.04448.
- [22] V. K. Goyal. Theoretical foundations of transform coding. *IEEE Signal Process. Mag.*, 18(5): 9–21, Sept. 2001.
- [23] D. He, Y. Zheng, B. Sun, Y. Wang, and H. Qin. Checkerboard context model for efficient learned image compression, 2021. URL https://arxiv.org/abs/2103.15306.
- [24] K. He, X. Zhang, S. Ren, and J. Sun. Deep residual learning for image recognition. In Proceedings of the IEEE Conference on Computer Vision and Pattern Recognition (CVPR), 2016.
- [25] D. Hendrycks and T. Dietterich. Benchmarking neural network robustness to common corruptions and perturbations. In *International Conference on Learning Representations*, 2019. URL https://openreview.net/forum?id=HJz6tiCqYm.
- [26] D. Hendrycks*, N. Mu*, E. D. Cubuk, B. Zoph, J. Gilmer, and B. Lakshminarayanan. Augmix: A simple method to improve robustness and uncertainty under data shift. In *International Conference on Learning Representations*, 2020. URL https://openreview.net/forum?id=S1gmrxHFvB.
- [27] D. Hendrycks, S. Basart, N. Mu, S. Kadavath, F. Wang, E. Dorundo, R. Desai, T. Zhu, S. Parajuli, M. Guo, D. Song, J. Steinhardt, and J. Gilmer. The many faces of robustness: A critical analysis of out-of-distribution generalization. In 2021 IEEE/CVF International Conference on Computer Vision (ICCV), pages 8320–8329, 2021. doi: 10.1109/ICCV48922.2021.00823.

- [28] A. Hepburn, V. Laparra, R. Santos-Rodriguez, J. Ballé, and J. Malo. On the relation between statistical learning and perceptual distances. In *International Conference on Learning Representations*, Mar. 2022.
- [29] I. M. P. E. G. M. ITU-T, Video Coding Experts Group (VCEG). Versatile video coding (h.266/vvc) standard. In *ITU-T Recommendation H.266 and ISO/IEC 23090-3*. International Telecommunication Union (ITU) and International Organization for Standardization (ISO) / International Electrotechnical Commission (IEC), 2020. URL https://www.itu.int/rec/ T-REC-H.266.
- [30] N. Johnston, E. Eban, A. Gordon, and J. Ballé. Computationally efficient neural image compression. arXiv preprint arXiv:1912.08771, 2019.
- [31] K. Kireev, M. Andriushchenko, and N. Flammarion. On the effectiveness of adversarial training against common corruptions. In *The 38th Conference on Uncertainty in Artificial Intelligence*, 2022. URL https://openreview.net/forum?id=BcU_UIIjqg9.
- [32] S. Klasky, J. Thayer, and H. Najm. Data reduction for science: Brochure from the advanced scientific computing research workshop. Technical report, Oak Ridge National Lab.(ORNL), Oak Ridge, TN (United States); SLAC National Lab., 2021.
- [33] E. Kodak. Kodak lossless true color image suite (PhotoCD PCD0992). URL http://r0k.us/graphics/kodak.
- [34] D. Kunin, J. Bloom, A. Goeva, and C. Seed. Loss Landscapes of Regularized Linear Autoencoders. In *Proceedings of the 36th International Conference on Machine Learning*, pages 3560–3569. PMLR, May 2019.
- [35] A. B. Lee, D. Mumford, and J. Huang. Occlusion Models for Natural Images: A Statistical Study of a Scale-Invariant Dead Leaves Model. *International Journal of Computer Vision*, 41 (1):35–59, Jan. 2001. ISSN 1573-1405. doi: 10.1023/A:1011109015675.
- [36] E. Lei, H. Hassani, and S. S. Bidokhti. Out-of-distribution robustness in deep learning compression. *arXiv preprint arXiv:2110.07007*, 2021.
- [37] L. Li, Z. Yang, and R. Wang. Improving multi-generation robustness of learned image compression, 2022.
- [38] T. Liang, J. Glossner, L. Wang, S. Shi, and X. Zhang. Pruning and quantization for deep neural network acceleration: A survey. *Neurocomputing*, 461:370–403, 2021. ISSN 0925-2312. doi: https://doi.org/10.1016/j.neucom.2021.07.045. URL https://www.sciencedirect.com/science/article/pii/S0925231221010894.
- [39] K. Liu, D. Wu, Y. Wang, D. Feng, B. Tan, and S. Garg. Malice: Manipulation attacks on learned image compression, 2022.
- [40] A. Luo, H. Sun, J. Liu, and J. Katto. Memory-efficient learned image compression with pruned hyperprior module, 2022. URL https://arxiv.org/abs/2206.10083.
- [41] M. C. Malin, M. A. Ravine, M. A. Caplinger, F. Tony Ghaemi, J. A. Schaffner, J. N. Maki, J. F. Bell III, J. F. Cameron, W. E. Dietrich, K. S. Edgett, et al. The mars science laboratory (msl) mast cameras and descent imager: Investigation and instrument descriptions. *Earth and Space Science*, 4(8):506–539, 2017.
- [42] D. Minnen, J. Ballé, and G. D. Toderici. Joint autoregressive and hierarchical priors for learned image compression. In S. Bengio, H. Wallach, H. Larochelle, K. Grauman, N. Cesa-Bianchi, and R. Garnett, editors, *Advances in Neural Information Processing Systems*, volume 31. Curran Associates, Inc., 2018. URL https://proceedings.neurips.cc/paper/2018/file/53edebc543333dfbf7c5933af792c9c4-Paper.pdf.
- [43] D. Mishra, S. K. Singh, and R. K. Singh. Deep architectures for image compression: A critical review. Signal Processing, 191:108346, 2022. ISSN 0165-1684. doi: https://doi.org/10.1016/ j.sigpro.2021.108346. URL https://www.sciencedirect.com/science/article/pii/ S0165168421003832.

- [44] S. Narang, G. F. Diamos, S. Sengupta, and E. Elsen. Exploring sparsity in recurrent neural networks. *CoRR*, abs/1704.05119, 2017. URL http://arxiv.org/abs/1704.05119.
- [45] E. Perez, F. Strub, H. de Vries, V. Dumoulin, and A. Courville. Film: Visual reasoning with a general conditioning layer. *Proceedings of the AAAI Conference on Artificial Intelligence*, 32 (1), Apr. 2018.
- [46] E. Plaut. From Principal Subspaces to Principal Components with Linear Autoencoders, Dec. 2018.
- [47] J. Rissanen and G. Langdon. Universal modeling and coding. *IEEE Transactions on Information Theory*, 27(1):12–23, 1981. doi: 10.1109/TIT.1981.1056282.
- [48] H. Sun, L. Yu, and J. Katto. End-to-end learned image compression with quantized weights and activations, 2021. URL https://arxiv.org/abs/2111.09348.
- [49] J. Sun, A. Mehra, B. Kailkhura, P.-Y. Chen, D. Hendrycks, J. Hamm, and Z. M. Mao. A spectral view of randomized smoothing under common corruptions: Benchmarking and improving certified robustness. In *Computer Vision–ECCV 2022: 17th European Conference, Tel Aviv, Israel, October 23–27, 2022, Proceedings, Part IV*, pages 654–671. Springer, 2022.
- [50] J. Sun, Q. Zhang, B. Kailkhura, Z. Yu, C. Xiao, and Z. M. Mao. Benchmarking robustness of 3d point cloud recognition against common corruptions. arXiv preprint arXiv:2201.12296, 2022.
- [51] L. Theis, W. Shi, A. Cunningham, and F. Huszár. Lossy image compression with compressive autoencoders, 2017. URL https://arxiv.org/abs/1703.00395.
- [52] G. Toderici, W. Shi, R. Timofte, L. Theis, J. Balle, E. Agustsson, N. Johnston, and F. Mentzer. Workshop and challenge on learned image compression (clic2020), 2020. URL http://www.compression.cc.
- [53] Z. Wang and A. C. Bovik. Mean squared error: Love it or leave it? a new look at signal fidelity measures. *IEEE signal processing magazine*, 26(1):98–117, 2009.
- [54] Z. Wang, A. Bovik, H. Sheikh, and E. Simoncelli. Image quality assessment: from error visibility to structural similarity. *IEEE Transactions on Image Processing*, 13(4):600–612, 2004. doi: 10.1109/TIP.2003.819861.
- [55] Z. Wang, A. C. Bovik, H. R. Sheikh, and E. P. Simoncelli. Image quality assessment: from error visibility to structural similarity. *IEEE transactions on image processing*, 13(4):600–612, 2004.
- [56] A. Wieckowski, J. Brandenburg, T. Hinz, C. Bartnik, V. George, G. Hege, C. Helmrich, A. Henkel, C. Lehmann, C. Stoffers, I. Zupancic, B. Bross, and D. Marpe. Vvenc: An open and optimized vvc encoder implementation. In *Proc. IEEE International Conference on Multimedia Expo Workshops (ICMEW)*, pages 1–2. doi: 10.1109/ICMEW53276.2021.9455944.
- [57] F. Yang, L. Herranz, Y. Cheng, and M. G. Mozerov. Slimmable compressive autoencoders for practical neural image compression. In *Proceedings of the IEEE/CVF Conference on Computer Vision and Pattern Recognition (CVPR)*, pages 4998–5007, June 2021.
- [58] D. Yin, R. G. Lopes, J. Shlens, E. D. Cubuk, and J. Gilmer. A Fourier Perspective on Model Robustness in Computer Vision. Curran Associates Inc., Red Hook, NY, USA, 2019.
- [59] S. Yin, C. Li, Y. Bao, and Y. Liang. Universal efficient variable-rate neural image compression, 2021. URL https://arxiv.org/abs/2111.11305.
- [60] S. Yin, C. Li, W. Tan, Y. Bao, Y. Liang, and W. Liu. Exploring structural sparsity in neural image compression, 2022. URL https://arxiv.org/abs/2202.04595.
- [61] D. Zhang, J. Yang, D. Ye, and G. Hua. Lq-nets: Learned quantization for highly accurate and compact deep neural networks. In *Proceedings of the European Conference on Computer Vision (ECCV)*, September 2018.

- [62] M. Zhu and S. Gupta. To prune, or not to prune: Exploring the efficacy of pruning for model compression. In 6th International Conference on Learning Representations, ICLR 2018, Vancouver, BC, Canada, April 30 May 3, 2018, Workshop Track Proceedings. OpenReview.net, 2018. URL https://openreview.net/forum?id=Sy1iIDkPM.
- [63] X. Zhu, J. Song, L. Gao, F. Zheng, and H. T. Shen. Unified multivariate gaussian mixture for efficient neural image compression. In *Proceedings of the IEEE/CVF Conference on Computer Vision and Pattern Recognition (CVPR)*, pages 17612–17621, June 2022.

A Background and Related Work

A.1 Neural Image Compression (NIC)

In lossy image compression, an input image is compressed into a small file or bitstream for transmission or storage. This file is then used to reconstruct the original image. Several models have been proposed for neural (or learned) image compression such as convolutional neural networks (CNNs), autoencoders, and generative adversarial networks [22, 8, 9, 42, 51, 13, 57, 63, 43]. In the most basic version of these models, an image vector \mathbf{x} is mapped to a latent representation \mathbf{y} using a convolutional autoencoder. \mathbf{y} is then quantized into $\hat{\mathbf{y}}$, so it can be compressed to a bitstream via an entropy coding method, such as arithmetic coding [47]. During reconstruction, the received bits go through the reverse entropy coding process and the revealed $\hat{\mathbf{y}}$ is fed into a CNN decoder which outputs the reconstructed image $\hat{\mathbf{x}}$. These models can be trained end-to-end by using differentiable proxies of entropy coding [8].

Normally entropy coding relies on one prior probability model of \hat{y} , which is learned from the entire set of images. Ballé et al. [9], however, recognized that the prior of this model can be optimized for each image separately. By adding an additional hyperprior autoencoder to their model, they learn the latent representation for the entropy model of each image. The information transmitted from this autoencoder can be seen as equivalent to "side information" used by other codecs. Minnen et al. [42] further improved this model by adding an autoregressive prior to the hierarchicial prior used by Ballé.

A.2 Variable-Rate NIC

NIC models are trained using a loss of the form $R + \lambda D$ where R represents the compression bitrate, D represents the distortion in the reconstructed image (e.g., PSNR), and λ specifies the desired tradeoff. Generally NIC models are optimized for a single rate λ ; however, some work has considered variable-rate models [51, 13, 57].

Dosovitskiy and Djolonga [17]'s observation of the computational redundancy involved in training separate models for the same task at different points along the rate-distortion curve resulted in their loss-conditional training (LCT) method to train a single model to adapt over a distribution of loss functions. They demonstrated that the scale hyper-prior NIC model proposed by Ballé et al. [9] can be transformed into a variable-rate model which works over a range of compression rates λ . Notably, Yang et al. [57] proposed models where the rate-distortion tradeoff is controlled by the size of a "slimmable layer". This resulted in significantly compressed models at lower rates; however, the size of the model increases with rate and the models at the highest rates are the same size as the original models.

A.3 Generalization and robustness in DNNs for classification

It is well known that deep neural networks (DNNs) are prone to overfitting to the specific data distribution they are trained on. Much recent work has focused on improving the robustness of DNNs to other distributions of data, including common image corruptions [26, 58]. CIFAR-10-C and ImageNet-C were proposed as a benchmark datasets to test the robustness of models to common image corruptions such as corruptions from weather, blur, and digital noise [25]. Methods for improving robustness include data-level techniques such as adding augmentations and algorithm-level techniques like using larger models or adversarial training. [26, 31, 27, 14].

Yin *et al.* study the effects of data augmentation and adversarial training on different corruptions using a Fourier analysis [58]. They analyze the CIFAR-10-C dataset and find that most augmentation methods help in the high-frequency domain, but hurt in the low-frequency domain. However, it is unknown how image compression affects corrupted images. We analyze how different types of image compression affect the Power Spectral Density (PSDs) of both clean and corrupted data.

A.4 Generalization and robustness with NIC models

There is a limited amount of work studying the generalization and robustness of NIC models. [36] formulates a problem for designing robust NIC models and train DNNs to be robust to two particular types of distributional shifts. They find a tradeoff between OOD robustness and IND performance. Our work is complementary to this work in that we provide additional metrics and OOD benchmarks

to analyze the robustness of various models in more detail. [39] studies NIC models' robustness to white-box and black-box adversarial attacks and proposes new models which improve the robustness of NIC to such attacks. Our work instead looks at naturalistic distribution shifts, which is another important aspect of robustness [25].

[2] designed a NIC module which works on a specific set of OOD images. In particular, their module works on high dynamic range (HDR) images, despite being trained on mostly standard dynamic range (SDR) images. Although this is a specific example of testing NICs on OOD data, our work differs from theirs in that we analyze how NICs would perform on a wide variety of image corruptions without seeing any examples of these corruptions during training.

Additionally, [37] addresses the issue of "multi-generational loss", or the problem of a rapid degradation of quality as images are repeatedly encoded and decoded, with NIC models. Our work differs because we propose spectral tools to analyze the effects of one cycle of encoding and decoding and we study how this affects the performance of different downstream tasks. While multi-generation loss is an important area of study for tasks like image editing, we focus on analyzing the spectral distortions caused by one cycle of image compression and how these affect a model's generalization and robustness to OOD data. Furthermore, [37] proposes using JPEG2000 as a method to improve the robustness of classification tasks by compressing adversarial noise. We explore how NIC models compare to JPEG2000 in terms of their robustness to several common types of image corruptions.

A.5 Lightweight NIC via model pruning

In an effort to reduce the energy and compute cost required by deep neural networks (DNNs), much work has been devoted towards finding methods to approximate DNNs. Common approaches include pruning network weights or quantizing network weights and activations [19, 20, 44, 61, 38, 15]. Remarkably, large sparse models have been shown to outperform small dense models with the same number of weights [62]. Additionally, approximating DNNs can have benefits in terms of robustness on OOD data [16].

Nonetheless, limited efforts to prune or quantize NIC models have been explored. Recently, Gille et al. [21] successfully introduced structured sparsity into NIC models to simultaneously reduce storage and power costs while maintaining a similar rate-distortion curve when compared to a dense version of the same NIC architecture. Their findings produced $\sim 80\%$ reduction in the number of parameters and $\sim 30\%$ reduction in MAC operations required by the NIC encoder. Yin et al. [60] also explored the use of structured sparsity in NIC and their proposed ABCM method was demonstrated to provide up to $7\times$ and $3\times$ reduction in DNN parameters and inference time, respectively, with only a mild reduction to reconstruction quality. Luo et al. [40] proposed a technique for pruning NIC models that was demonstrated to maintain the same bpp as dense models but provided a parameter reduction of at most $\sim 34\%$. Sun et al. [48] demonstrated a technique for quantizing both NIC weights and activations to an 8-bit fixed point representation while yielding a rate-distortion curve comparable to the original 32-bit float NIC model. Outside of DNN pruning or quantization, alternative techniques have been explored for more efficient NIC [30, 59, 23].

A.6 Metrics for quantifying image compression quality

The objective of lossy image compression is to achieve a balance between minimizing 1) the size of the compressed file and 2) the distortion of the reconstructed image compared to the original image. As these objectives are inherently at odds, the performance of lossy image compression is typically measured using a rate-distortion curve, which measures the size of the compressed image (rate) versus the quality of the reconstructed image (distortion). The rate is usually measured in bits per pixel (bpp), which is the average number of bits required to store each pixel in the compressed representation. The distortion is usually measured by scalar metrics such as peak signal-to-noise ratio (PSNR) or a visual similarity metric such as MS-SSIM [54].

A.7 Benchmark datasets

We utilize two benchmark datasets for evaluating performance of our NIC models. For training and testing, we make use of CLIC (Challenge on Learned Image Compression) 2020 [52]. This collection is comprised of 1633 training, 102 validation, and 428 test images. The images are of varying

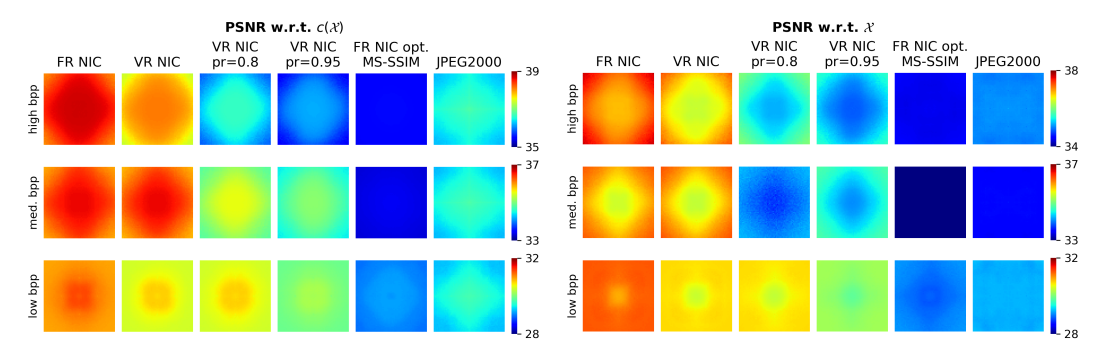


Figure 6: Fourier heatmaps of methods under the fixed-bpp setting. Left: PSNRs of $\mathcal{C}(c(\mathcal{X}))$ with respect to $c(\mathcal{X})$. Right: PSNR of $\mathcal{C}(c(\mathcal{X}))$ with respect to \mathcal{X} . Warmer colors (red) indicate higher PSNR.

resolution and are further categorized as either professional or mobile. To evaluate generalization, we make use of the Kodak [33] dataset which consists of 24 images of resolution 768×512 (or 512×768).

B Additional results: Fourier heatmaps

While our spectral tools allow us to measure different capabilities of compression models, they require the availability of OOD, or corrupted, data. To support a setting in which such OOD data is unavailable, we propose adopting another tool: the Fourier sensitivity heatmap. This tool evaluates the PSNR of a compression model on data perturbed with Fourier basis elements [58]. The resulting visualization is a heatmap where the value at coordinate (i,j) is the PSNR of the compression method on perturbed data $\{X_k + r_k \varepsilon U_{i,j}\}_{k=1}^N$, where each r_k is selected uniformly at random from $\{-1,1\}$, ε is the norm of the perturbation, and $U_{i,j}$ is the (i,j)th Fourier basis matrix. From [58], $U_{i,j} \in \mathbb{R}^{n_1 \times n_2}$ and satisfies $(i) \|U_{i,j}\| = 1$ and $(ii) \mathcal{F}(U_{i,j})$ has at most two non-zero coordinates specifically at (i,j) and the coordinate symmetric to (i,j) about the matrix center.

We consider two versions of Fourier heatmaps: (a) with respect to perturbed data and (b) with respect to original data. To analyze (a) and (b), the PSNR at each coordinate (i,j) is computed with respect to the perturbed dataset, $\{X_k + r_k \varepsilon U_{i,j}\}_{k=1}^N$, and the unperturbed dataset, $\{X_k\}_{k=1}^N$, respectively. (a) and (b) can be seen as measures of generalization and robustness respectively.

We computed Fourier heatmaps over the CLIC dataset in Figure 6. We selected hyper-parameters for these models using a fixed-bpp constraint on the clean data. We also show results under a fixed-PSNR constraint in Appendix 22. Note: in these Fourier heatmap plots, warmer colors represent *higher PSNR*, which is in contradiction to the plots of \mathcal{D} , \mathcal{G} , and \mathcal{R} where warmer colors represented *more error*.

On the left side of Figure 6, we analyze the generalization of the image compression models to various frequency shifts. We find that all image compression models generalize to low and medium-frequency signals better than high-frequency signals. Specifically, observe how the centers of the plots—corresponding to low-frequency signals—have hotter colors than the edges of the plots. This corroborates our findings from both the RD curves and \mathcal{G} metrics on the CLIC-C dataset in Section 4.2 and Appendix G. For FR NIC opt. MS-SSIM, this difference is only noticeable at the lowest bpp; however for the other models, there is a clear difference in performance for low and high-frequency shifts at all bpps. Additionally, the effect of pruning is a degradation in PSNR at all frequencies.

On the right side of Figure 6, we analyze the robustness, or denoising, capabilities of the models. These plots show that NIC models are better at denoising high-frequency corruptions than low-frequency corruptions (notice the cooler-colored diamonds in the center of the NIC plots). Meanwhile JPEG2000 has very consistent and poor denoising properties across the entire range of corruption frequencies (the plots are blue with a narrow gradient of color compared to the NIC plots). According to this metric, NIC opt. MS-SSSIM also has poor denoising capabilities (the plots are all dark blue compared to the NIC plots) and pruning NICs also results in a degradation of denoising performance. At first, this may seem like a contradiction to our downstream classification results from Appendix C,

which showed that NIC opt. MS-SSIM and VR NIC pr=0.8/0.95 were more effective at denoising high-frequency corruptions than FR NIC and VR NIC. However, recall that each pixel in these plots only shows the *average PSNR* of the entire perturbed dataset as opposed to the spectral error by frequency, like our \mathcal{D} , \mathcal{G} , and \mathcal{R} plots show. Then from the main body and Appendix H, it is clear that this PSNR metric is not detailed enough highlight the nuances between the spectral distortion patterns of different methods.

C Additional results: pruned NIC models and NIC models optimized for MS-SSIM

In this section, we analyze more comprehensive set of NIC variants. In particular, we consider NICs which have been pruned and NICs which are optimized for MS-SSIM (as opposed to PSNR). To prune our variable-rate NIC models, we use a gradual magnitude pruning (GMP) [62] based approach which has been demonstrated to effectively sparsify DNNs. At a high level, GMP gradually prunes DNN weights based on their magnitude over a fixed number of epochs then continues to train, or fine-tune, the remaining sparse network after the target sparsity is reached. More details of the GMP algorithm are provided in Appendix K.

Below are descriptions of the two variants we add:

- 1. **VR NIC pr=0.8/0.95:** One <u>variable-rate</u> model trained over a continuous range of λ values. Distortion is MSE. Here, GMP is applied during training to prune 80% or 95% of the convolutional *and* FiLM weights.
- 2. **FR NIC opt. MS-SSIM:** Eight dense fixed-rate models trained over 8 different λ values. Distortion is (1 MS-SSIM) (*i.e.*, model is optimized for MS-SSIM).

Figures 7, 9, and 8 show results for these models. We discuss our findings below.

C.1 Evaluating spectral distortion on IND data

Effect of pruning. VR NIC, VR NIC pr=0.8, and VR NIC=0.95 all have the same VR NIC model architecture, but have 0%, 80%, and 95% sparsity respectively. The RD curves show that pruning causes a degradation in performance, especially for high bpp (see blue lines in Figure 7). However, the PSDs reveal that, even if we make up for the PSNR performance gap by increasing the bpp (right side of Figure 7), the pruned models left a different spectral artifacts from the dense ones. In particular, as the prune rate increases, the ring in the high-frequency region of the PSDs becomes thicker. Presumably reconstructing signals at high-frequencies requires more parameters than reconstructing low frequency signals and so the more sparse models focus on optimizing the "easier" frequencies on the spectrum. These results show that pruning NICs exacerbates the spectral differences between NIC and JPEG2000 that we observed in Figure 2.

Effect of optimization variable in NIC. The FR NIC and FR NIC opt. MS-SSIM have the same FR NIC model architecture, but optimize for different "distortion" metrics (*i.e.*, FR NIC optimizes for PSNR while FR NIC opt. MS-SSIM optimizes for MS-SSIM). Unsurprisingly, Figure 7 shows that the FR NIC opt. MS-SSIM model has the worst performance of all the models in terms of RD curves where the distortion metric is PSNR. However, the plots of the distortion error \mathcal{D} give us more insights into the spectral errors that this model is making. Surprisingly, FR NIC opt. MS-SSIM produces spectral artifacts which differ greatly from both the PSNR optimized NIC models and the classic JPEG2000 codec. In particular, like JPEG2000, this model distorts the medium and low frequencies more than high-frequencies (notice the cooler-colored ring around the hot-colored center). However, it differs from JPEG2000 in that it leaves a less rectangular artifact. Thus, the optimization objective of NIC can influence the spectral artifacts and should be thoroughly examined before being used in practice.

C.2 Robustness and generalization

We analyze the findings further using our robustness spectral inspection tools on ImageNet-C in Figure 8. The plots of $\mathcal G$ on the snow corruption show that although the models have different magnitudes of errors, all models leave similar magnitudes of errors across the frequency spectrum (*i.e.*, the gradient of each plot is narrow). Furthermore, all models have similar plots of $\mathcal R$. This

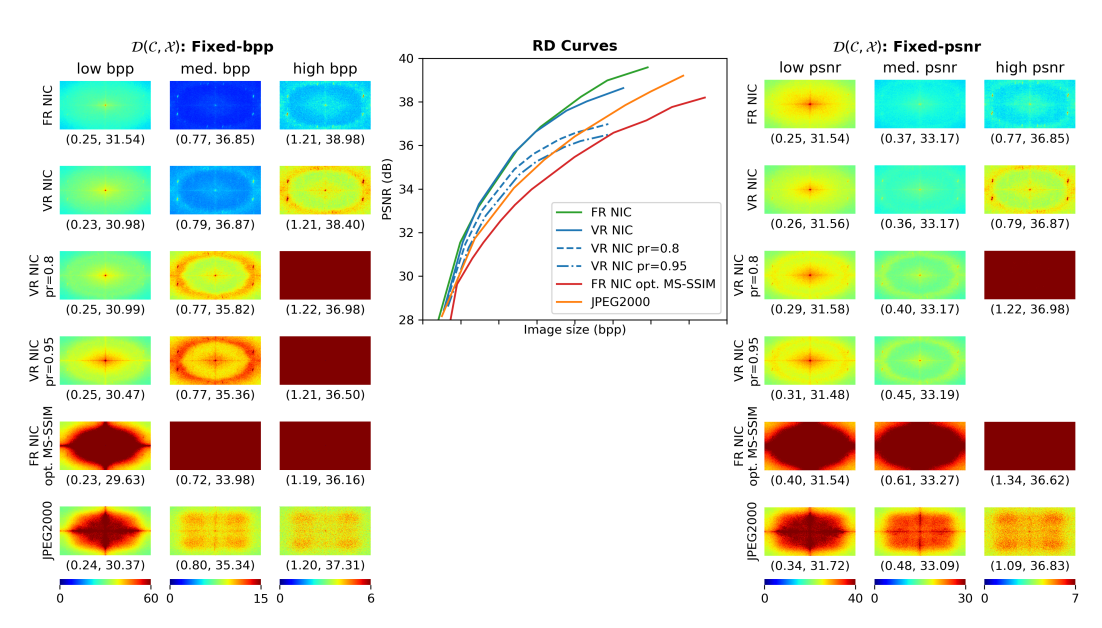


Figure 7: **Visualizing distortion via CLIC test set evaluation with NIC variants. Left:** spectral measure of in-distribution reconstruction error \mathcal{D} under the fixed-bpp constraint at three rates. **Center:** Rate-distortion curves with vertical lines indicating fixed-bpp values and horizontal lines indicating fixed-PSNR values. **Right:** \mathcal{D} under fixed-PSNR constraint. Each \mathcal{D} plot is labeled with a tuple of that model's (bpp, PSNR) on CLIC. Hotter colors (red) indicate more error in that frequency range.

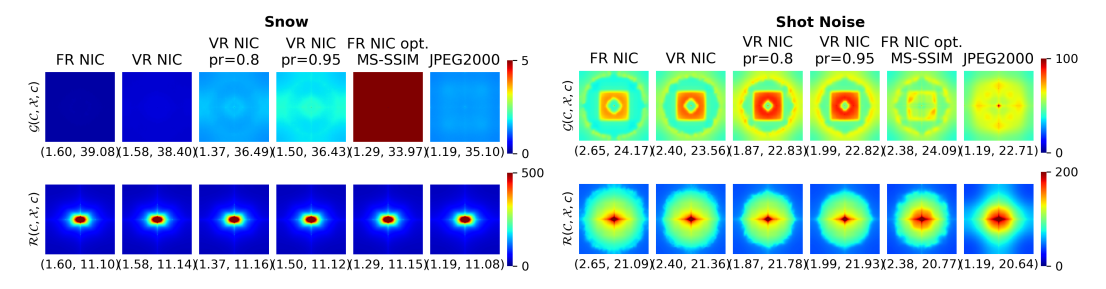


Figure 8: Spectral measures \mathcal{G} and \mathcal{R} for all NIC variants on two example corruptions of ImageNet-C. Model hyper-parameters were chosen such that they give bpp \approx 1.23 on ImageNet. Each plot is labeled with the model's bpp and PSNR with respect to $c(\mathcal{X})$ (top row) or \mathcal{X} (bottom row).

follows the result of the next section (accuracy on the downstream task), which shows that all six models have comparable accuracies at this compression rate (see snow column of bpp \approx 1.23 plot in Figure 9).

On the shot noise corruption, however, we see some notable differences between models on both \mathcal{G} and \mathcal{R} . On \mathcal{G} , we see that as the prune rate increases, the ring of high-frequency spectral error becomes significantly more bold. This reiterates our finding from Figure 7 that pruning results in a degradation of high-frequency signal reconstruction. Similarly, FR NIC opt. MS-SSIM has a thicker ring than FR NIC in the high-frequency domain. Interestingly, this model also has a smaller error in the low frequency domain compared to the NIC models optimized for PSNR. Finally, JPEG2000 distorts low- and medium-frequencies relatively evenly and distorts high-frequency signals less than NIC which follows from Section 4.1. We can see the effect of these differences in \mathcal{G} in the high-frequency domain of of the plots \mathcal{R} . Specifically, the VR NIC leaves a slightly smaller artifact than FR NIC (*i.e.*, the circle of warm colors is larger with VR NIC). This differences is exacerbated as the prune rate increases (*i.e.*, NIC pr=0.95 has the smallest artifact of the four first four models), which suggests that the pruned NIC models are most effective for denoising high-frequency corruptions. FR NIC opt. MS-SSIM also leaves a smaller artifact than FR NIC; however, this has a different shape than the NIC models optimized for PSNR (specifically, there are jagged edges on the edges of this

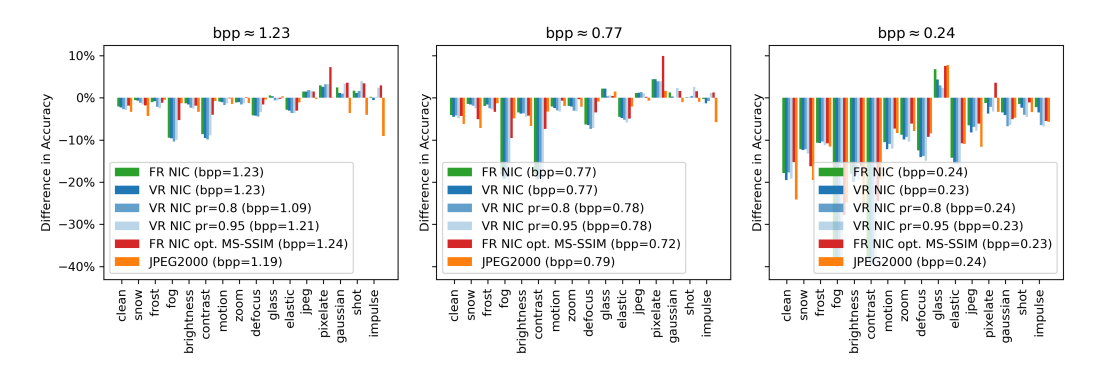


Figure 9: Effect of compressing corrupt images on classification accuracy. Each subplot displays the difference in top-1 accuracy after compressing corrupt images at a different compression rate (bpp=1.23, 0.77, and 0.24). Specifically, let A(X) be the top-1 accuracy of the model on dataset X, measured in percentage points. We report $A(\mathcal{C}(c(X))) - A(c(X))$ over all -C corruptions (or on clean ImageNet in the case of "clean"). Each subplot shows results under a different fixed-bpp constraint based on the bpps achieved by the compressors on the clean ImageNet dataset.

artifact). This suggests that FR NIC opt. MS-SSIM denoises high-frequency data better than FR NIC, but in a different way from VR NIC pr=0.8/0.95. Finally, JPEG2000 has diamond-shaped artifact which suggests it denoises some high-frequency signals, but not all.

C.3 Downstream task

We also consider how these NIC variants perform on the same downstream classification task outlined in Section 4.3. Figure 9 shows the difference in accuracy before and after corruption for each model on each corruption (or clean data) and Appendix N has tables with these accuracies. We find that these variants are even better at denoising high-frequency corruptions than the dense FR and VR NICs that we tested in the main body. In particular, we find that on the high-frequency corruptions at bpp = 1.23 and 0.77, the pruned VR NICs show a *larger improvement in accuracy* than the dense VR and FR NICs. This finding matches our observation in Figure 7 that the pruned NICs denoise high-frequency signals even more than dense NICs, who in turn denoise these signals more than JPEG2000. The pruned models perform comparably to the dense models on low- and medium-frequency corruptions. Similarly, we also find that NIC opt. MS-SSIM also improves performance on the downstream task on high-frequency corruptions over (a) no compression and (b) compression with dense NIC models. This model also has better performance than the other NIC variants and low- and medium-frequency corruptions.

D \mathcal{G} and \mathcal{R} for FR and VR NIC on CLIC

Figure 10 shows that VR NIC and FR NIC have very similar \mathcal{G} and \mathcal{R} plots on the three representative frequency shifts.

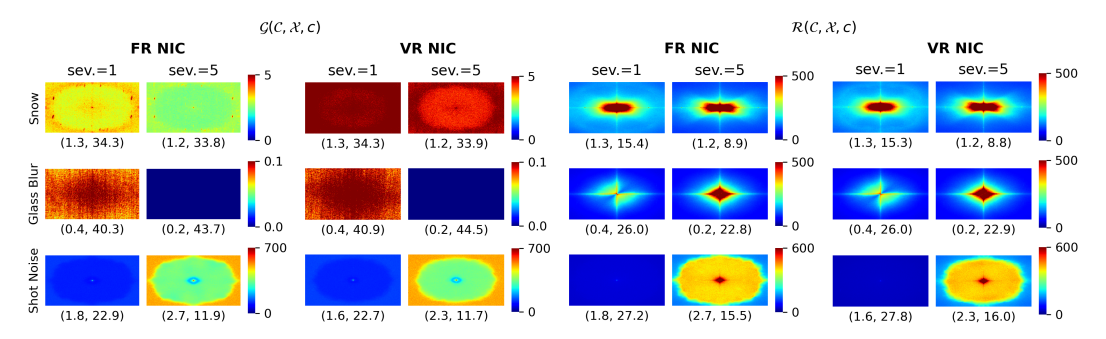


Figure 10: Generalization error \mathcal{G} and denoising error \mathcal{R} for FR and VR NIC (results for VR NIC were omitted from main body due to space constraints). We plot both spectral metrics for one low, medium, and high-frequency corruption at severities 1 and 5. Each plot is labeled with a tuple of that model's (bpp, PSNR) on the CLIC-C dataset with that corruption.

E Additional results: comparing JPEG2000 and VTM

In this section, we compare two classical codecs: JPEG2000 and Versatile Video Coding (VVC) (also known as h.266) codec [29]. We used VTM software from [56] and implementation from [10] to test h.266, which we refer to as "VTM". Although VTM has state-of-the-art performance for classical codecs, we chose to use JPEG2000 as the representative classical codec in the main body for three reasons.

- 1. **JPEG2000** has more consistent bpp usage. As shown later in this section (Figure 13), VTM varies its bpp usage drastically depending on the corruption type and severity. Specifically, a hyper-parameter which gives a bpp of x on clean data may give a bpp of over 7x on certain OOD shifts and severities. Thus, it was unclear how to fairly compare VTM and NIC in a fixed-bpp setting on OOD data.
- JPEG2000 implementation has faster inference time. The current open-source implementation
 for VTM is significantly slower than those available for JPEG2000 (10s to 100s of seconds for
 VTM vs. < 1 second for JPEG2000). Thus, JPEG2000 was a more feasible codec for our extensive
 experimentation.
- 3. After adjusting for PSNR, VTM shows similar spectral results as JPEG2000. Finally, although there are differences in magnitudes of the spectral distortion plots, JPEG2000 and VTM exhibit similar patterns, so we found it sufficient to use only one classical codec representative.

We include results comparing JPEG2000 and VTM on the Kodak and Kodak-C datasets in Figures 11, 12, 13, and 14 and explain our findings below.

E.1 Evaluating VTM on IND data

Figure 11 is analogous to Figure 2 in the main body. From the RD curves, we see that VTM outperforms FR NIC and JPEG2000 across all tested bpps. VTM's plots of $\mathcal D$ are most similar to JPEG2000's. Specifically, at low compression rates (high bpp/PSNR), both methods leave similar errors across all frequencies (notice the small gradient of colors in both JPEG2000 and VTM's plots of $\mathcal D$ at med/high bpp and med/high PSNR). Similarly, at high compression rates (low bpp/PSNR) both models leave more spectral errors at the low and medium frequencies. Despite having similar patterns to JPEG2000, most of the VTM plots have a smaller magnitude than JPEG2000, even at fixed-PSNRs. This suggests that the metric $\mathcal D$ metric is more closely aligned with VTM's modus operandi than JPEG2000's.

Figure 12 shows the six VTM plots from Figure 11 without constrained color map scales. These results confirm that VTM leaves only a small magnitude of error, which is even across frequencies.

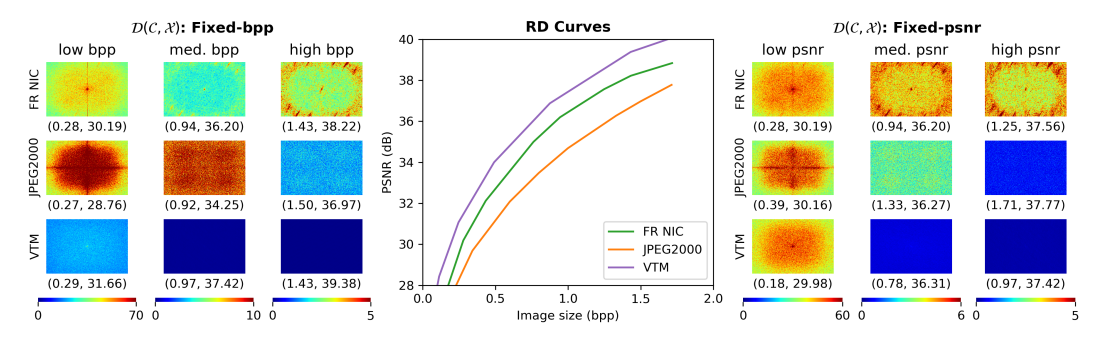


Figure 11: **Visualizing distortion of VTM via Kodak test set evaluation. Left:** spectral measure of in-distribution reconstruction error \mathcal{D} under the fixed-bpp constraint at three rates. **Center:** Rate-distortion curves with vertical lines indicating fixed-bpp values and horizontal lines indicating fixed-PSNR values. **Right:** \mathcal{D} under fixed-PSNR constraint. Each \mathcal{D} plot is labeled with a tuple of that model's (bpp, PSNR) on Kodak. Hotter colors (red) indicate more error in that frequency range.

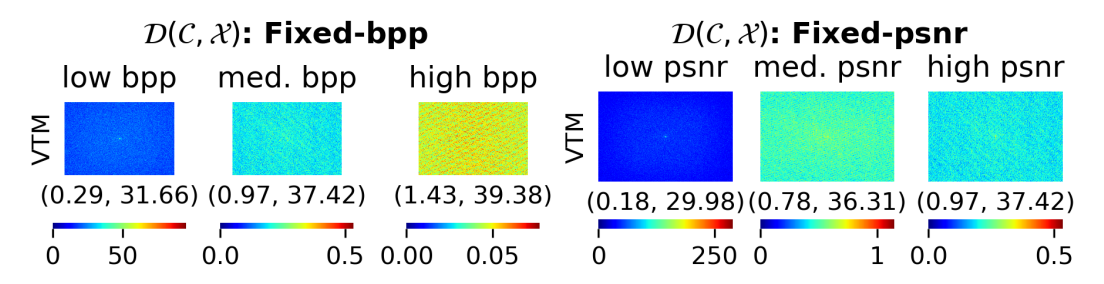


Figure 12: Unscaled plots of ${\cal G}$ and ${\cal R}$ with VTM from Figure 11.

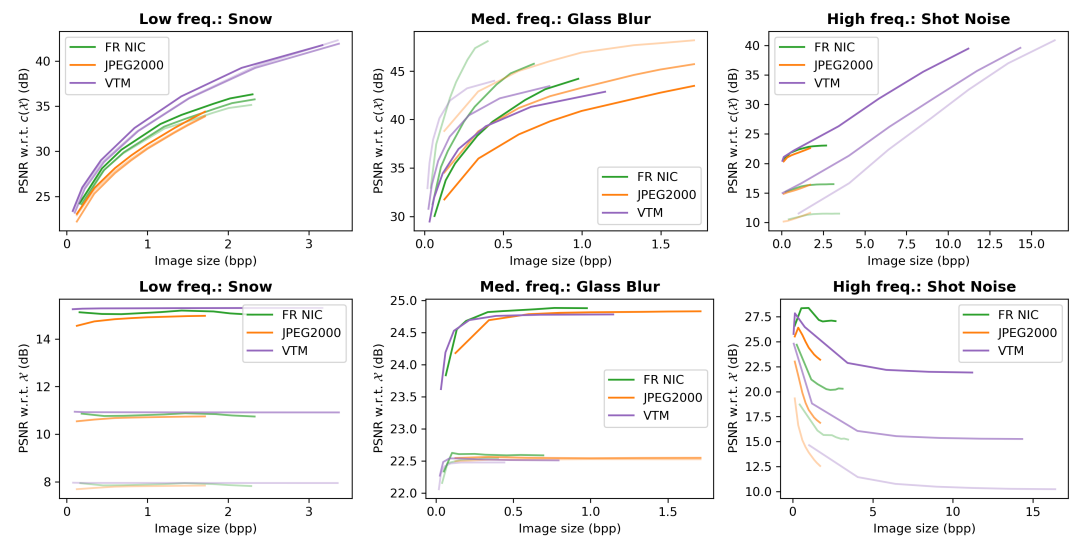


Figure 13: Rate-distortion curves for a representative low, medium, and high-frequency shift. Each shift and model has three curves for severity=1 (least transparent), severity=3, and severity=5 (most transparent). Top row: generalization of $C(c(\mathcal{X}))$ w.r.t. $c(\mathcal{X})$ (i.e., PSNR of the reconstructed shifted images w.r.t. the original shifted images). Bottom row: denoising of $C(c(\mathcal{X}))$ w.r.t. \mathcal{X} (i.e., PSNR of the reconstructed shifted images w.r.t. the original clean images).

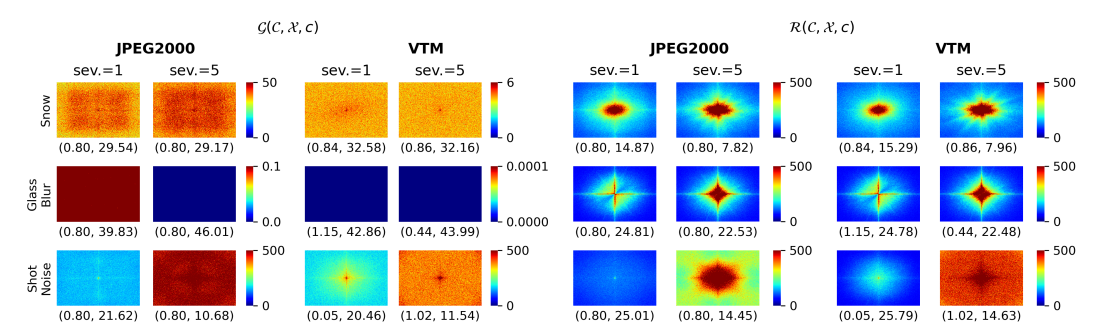


Figure 14: Generalization error \mathcal{G} and denoising error \mathcal{R} for JPEG2000 and VTM. We plot both spectral metrics for one low, medium, and high-frequency corruption at severities 1 and 5. Each plot is labeled with a tuple of that model's (bpp, PSNR) on the Kodak-C dataset with that corruption.

E.2 Evaluating VTM on OOD data

Figure 13 shows the RD curves of VTM on a low, medium, and high-frequency shift. On the low-frequency shift (snow), VTM has comparable performance to FR NIC and JPEG2000 at low bpp; however, VTM can achieve higher PSNRs by increasing its bpp usage. This finding suggests that VTM, like the other codecs in Section 4.2.1, generalizes well to low-frequency shifts. However, this highlights the fact that VTM may drastically increase its bpp usage on OOD data. Interestingly, all three models are comparably robust to the snow corruption (bottom row of Figure 13) and the severity of the corruption is the largest determinant of the PSNR with respect to \mathcal{X} .

On the medium-frequency shift (glass blur), VTM, like the other codecs in Section 4.2.1, achieves PSNRs which are higher than the PSNRs on clean data. However, VTM is not as effective as FR NIC in terms of PSNR with respect to $c(\mathcal{X})$ on this shift (the VTM curves start to flatten around 40-42 PSNR, while the NIC curves flatten around 42-47 PSNR). Like the snow corruption, all three models are comparably robust to the glass blur corruption (bottom row of Figure 13) and the severity of the corruption is the largest determinant of the PSNR with respect to \mathcal{X} .

On the high-frequency shift (shot noise), VTM displays a drastically different pattern from both NIC and JPEG2000. Specifically, VTM is able to achieve significantly higher PSNRs with respect to $c(\mathcal{X})$ (i.e., generalize better) than FR NIC and JPEG2000. However, this comes at a very serious cost in terms of bpp (notice the bpp range for shot noise in Figure 13 is 0-17 versus a typical range of 0-2). Recall that in Section 4.2.1 we observed that NIC models adjusted their bpp usage depending on the type of corruption—in particular, NIC models used more bpps than JPEG2000 on the shot noise corruption, even though it did not improve the PSNR. Figure 13 shows that VTM adjusts its bpp usage in a more extreme way than NIC models, but, unlike NIC models, this increase in bpp does result in an increase in PSNR with respect to $c(\mathcal{X})$. As expected from our results in Section 4.2.1, this increase in PSNR with respect to $c(\mathcal{X})$ results in a decrease of PSNR with respect \mathcal{X} . Overall, VTM's highly variable bpp usage could be a real disadvantage to using VTM in the wild: in particular, if a practitioner selects a hyper-parameter from clean data and expects the model will use a certain amount of bpps, VTM might use a much larger bpp than expected on OOD data. Thus, our OOD benchmark dataset is a vital aspect to comprehensive image compression testing.

Figure 14 shows the \mathcal{G} and \mathcal{R} metrics on the three representative shifts.⁶ On the snow corruption, VTM has a smaller magnitude of errors than JPEG2000 across all frequencies; however, both models leave relatively even errors across all frequencies and both models distort low frequencies more than high frequencies (which is the opposite as FR NIC on the snow corruption in Figure 4). At both severities, the two models have similar plots of \mathcal{G} . VTM is highly effective at reconstructing the glass blur– the magnitude of \mathcal{G} is <0.0001 across all frequencies— which matches our findings on the other codecs in Section 4.2.2. Additionally, JPEG2000 and VTM have nearly identical plots of \mathcal{R} at both

⁵For example, when q=17, VTM uses 2.32 bpp on Kodak and 16.49 bpp on Kodak-C shot noise with severity=5.

⁶Note that we select one hyper-parameter for JPEG2000 (q=15); however, we vary the hyper-parameter choice for VTM across corruptions (q=32, 17, 47 for snow, glass blur, and shot noise respectively) so that VTM gives bpps in the ballpark of 0.8 for each corruption.

severities. Finally, on the shot noise corruption, both JPEG2000 and VTM display similar magnitudes and patterns of errors. Both models leave significantly more error on $\mathcal G$ at severity=5 than severity=1; however, JPEG2000 maintains a bpp=0.8 at both severities while VTM increases its bpp from 0.05 to 1.02. Additionally, unlike NIC, both of these models leave their highest errors in the low-frequency domain of $\mathcal G$. Lastly, both models are not as effective at denoising high-frequency signals as NIC proved to be.

F Additional results: Kodak and Kodak-C

This section contains Figures equivalent to those in the main body for the Kodak and Kodak-C dataset.

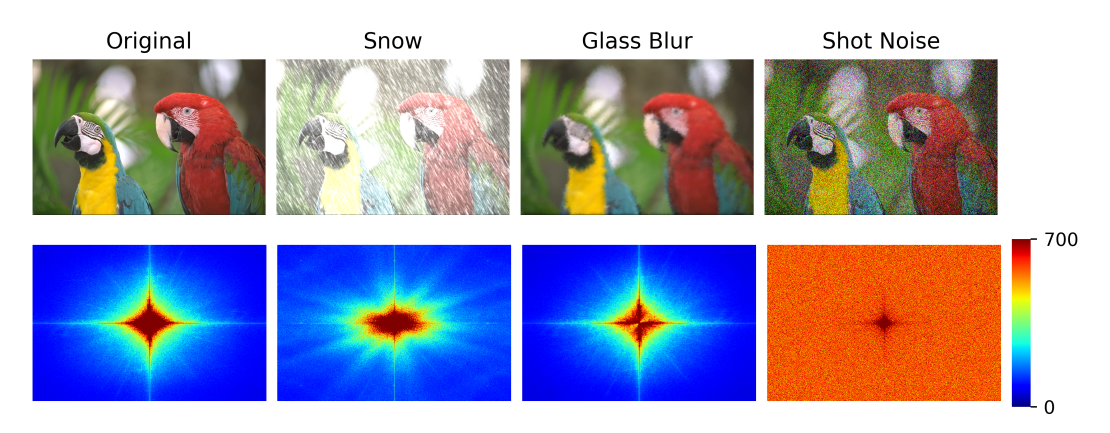


Figure 15: Figure equivalent to Figure 1a for Kodak-C dataset.

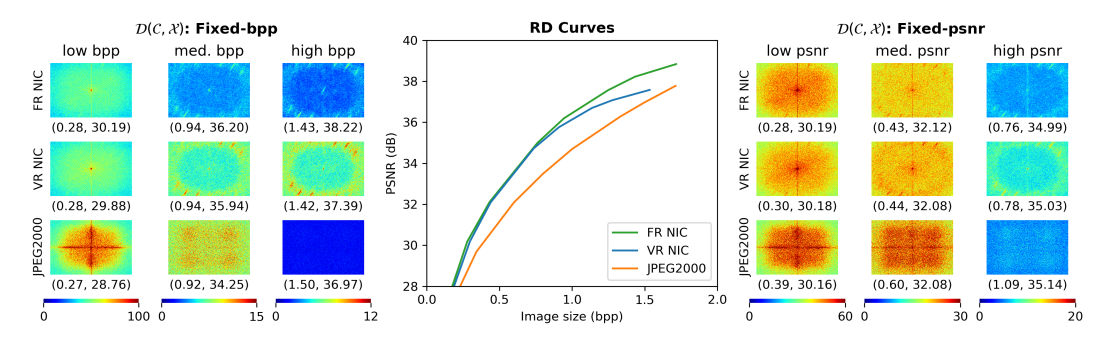


Figure 16: Figure equivalent to Figure 2 for Kodak dataset

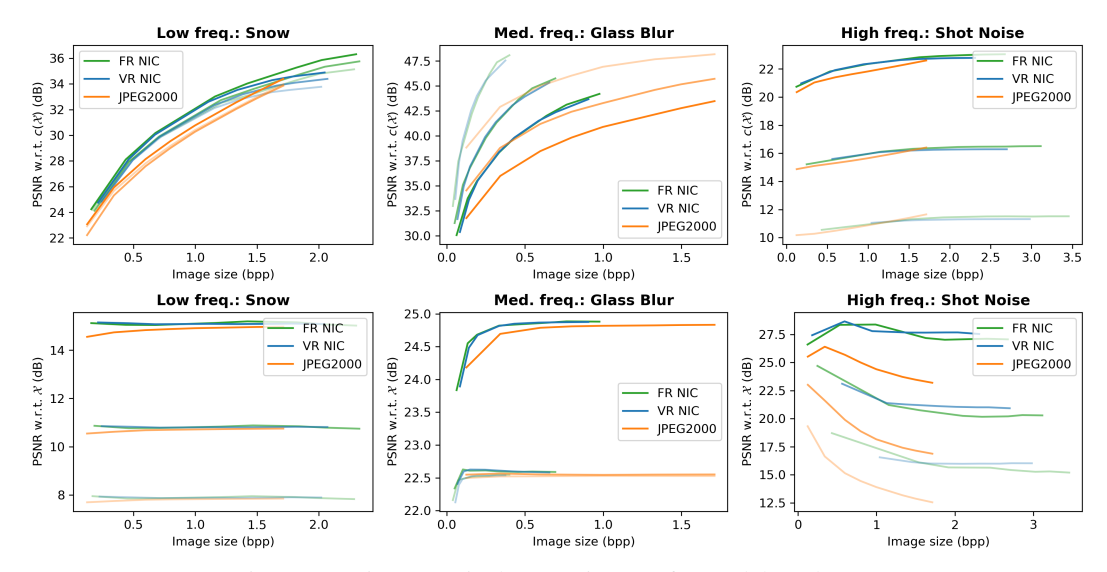


Figure 17: Figure equivalent to Figure 3 for Kodak-C dataset

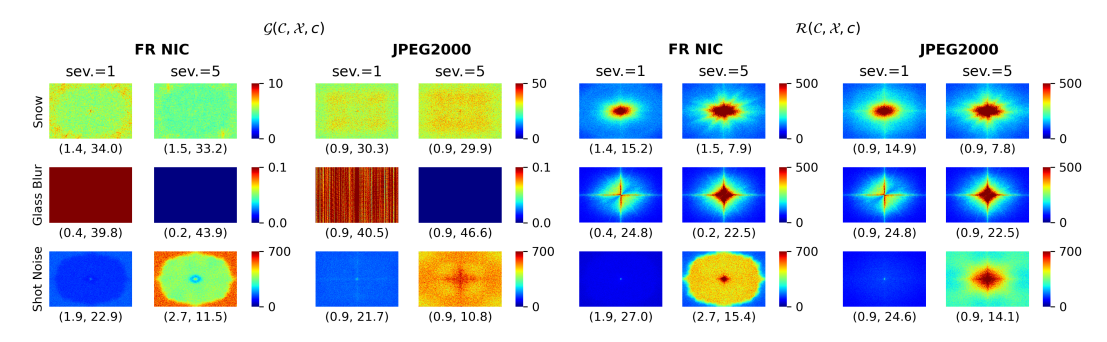


Figure 18: Figure equivalent to Figure 4 for Kodak-C dataset

G Additional results: other CLIC-C corruptions

Figures 19, 20, and 21 show the results of the other 12 corruptions from CLIC-C which were not included in the main body. Overall, we see that our three representative corruptions (snow, glass blur, and shot noise) represent the trends of the low, medium and high frequency corruptions well.

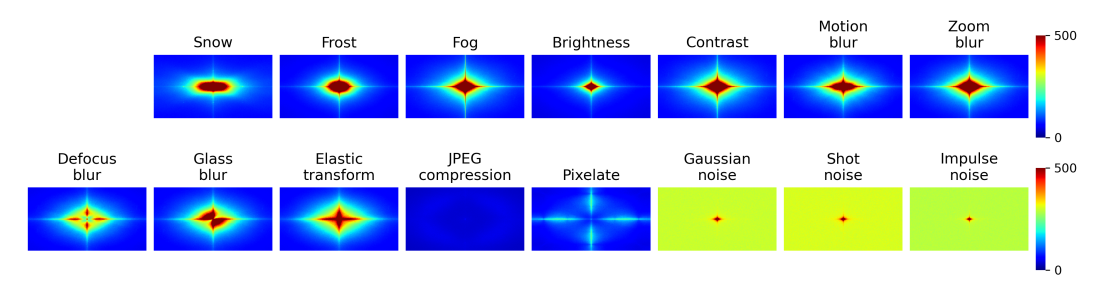


Figure 19: Average PSD of the difference between the corrupted images and the clean images for each given CLIC-C corruption c, $\frac{1}{N}\sum_{k=1}^{N}PSD(c(X_k)-X_k)$. Severity=5.

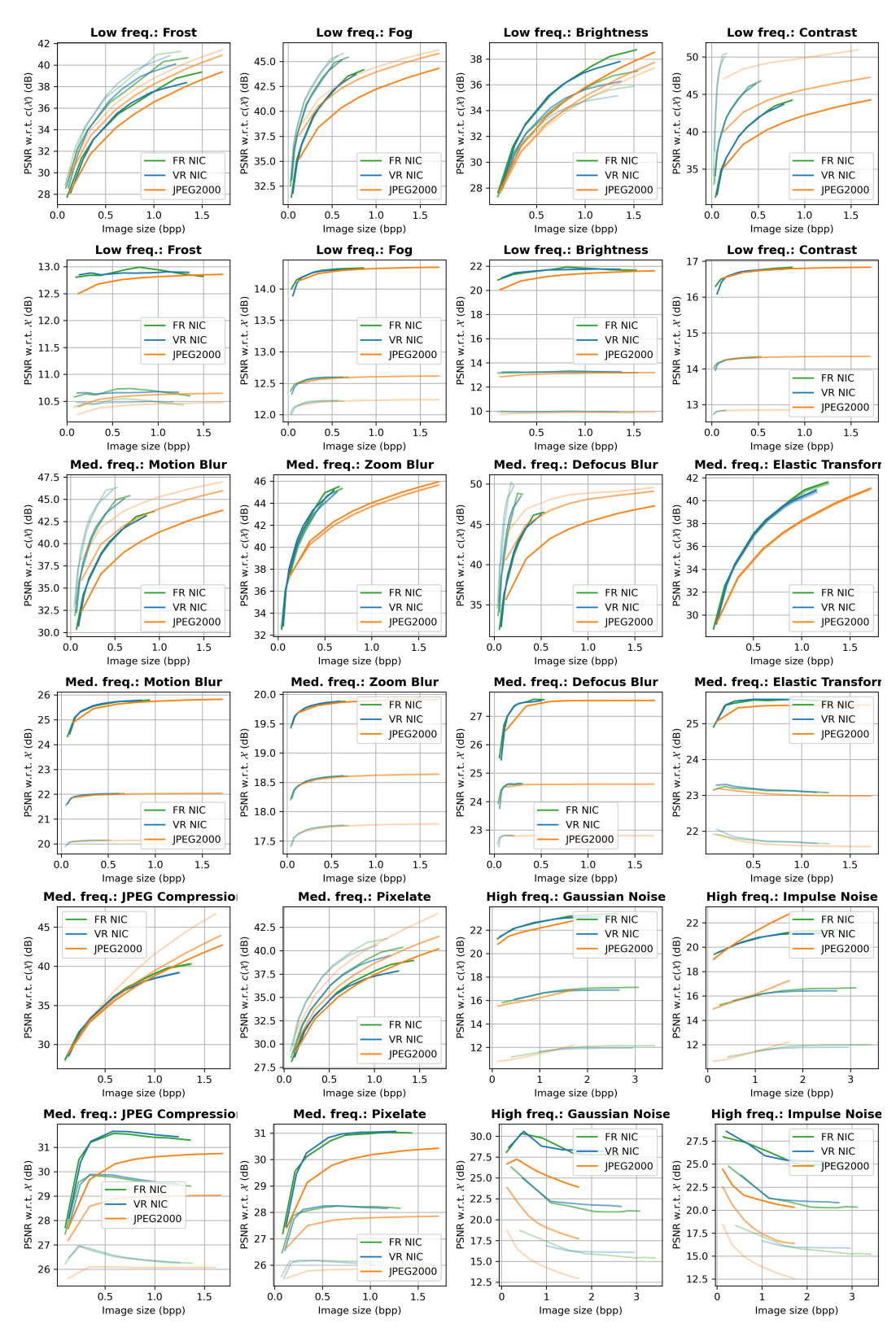


Figure 20: RD Curves for corruptions not seen in the main body. Rows 1, 3, and 5 show PSNR w.r.t. $c(\mathcal{X})$. Rows 2, 4, and 6 show PSNR w.r.t. \mathcal{X} .

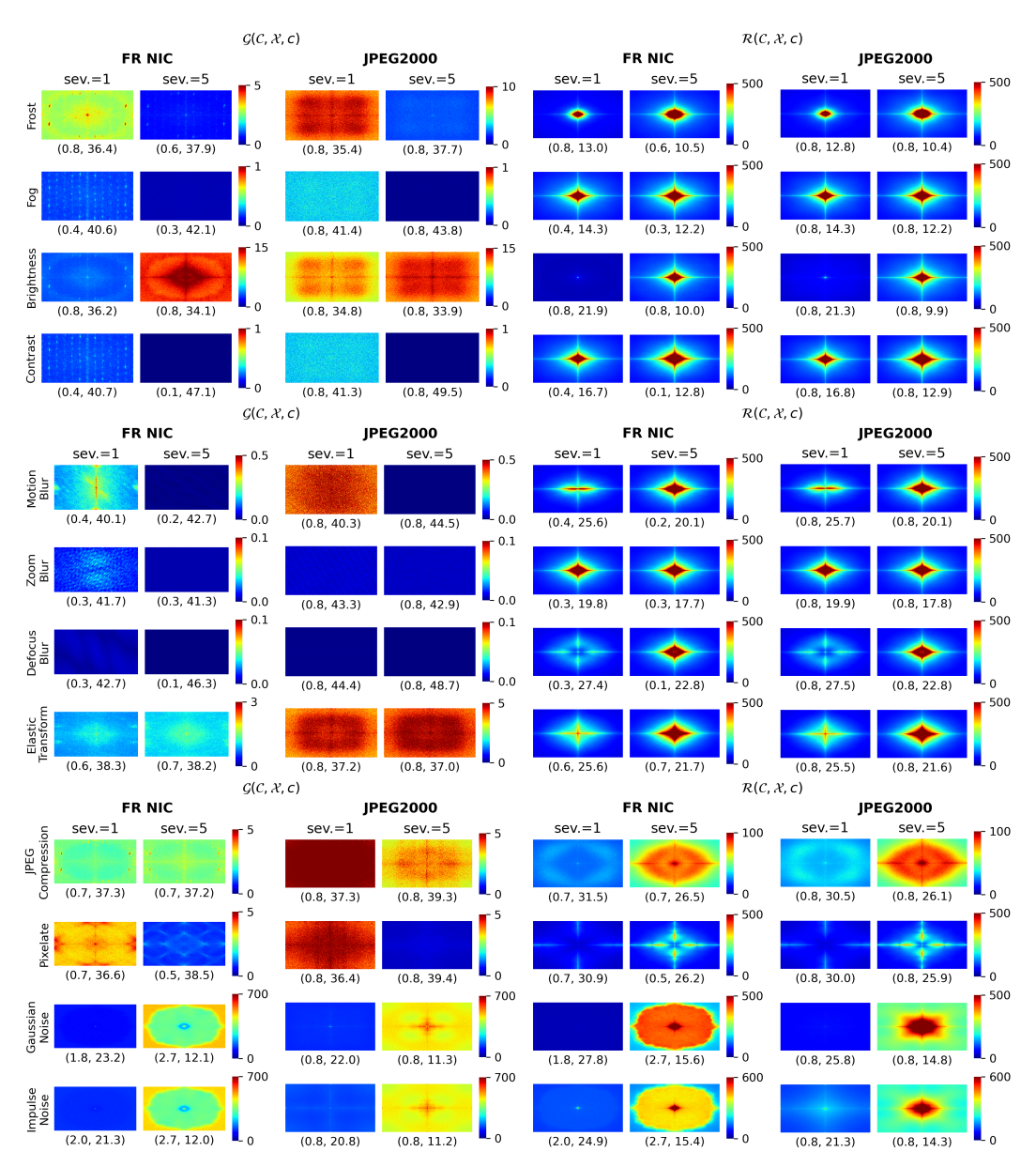


Figure 21: Generalization error $\mathcal G$ and denoising error $\mathcal R$ for FR NIC and JPEG2000 on other corruptions of CLIC-C. We plot both spectral metrics for one low, medium, and high-frequency corruption at severities 1 and 5. The plots of $\mathcal G$ and $\mathcal R$ are labeled with tuples of the model's (bpp, PSNR w.r.t. $c(\mathcal X)$) and (bpp, PSNR w.r.t. $\mathcal X$) respectively.

H Additional results: fixed-PSNR constraint

This section shows results of the Fourier Heatmaps and downstream classification tasks on a fixed-PSNR constraint.

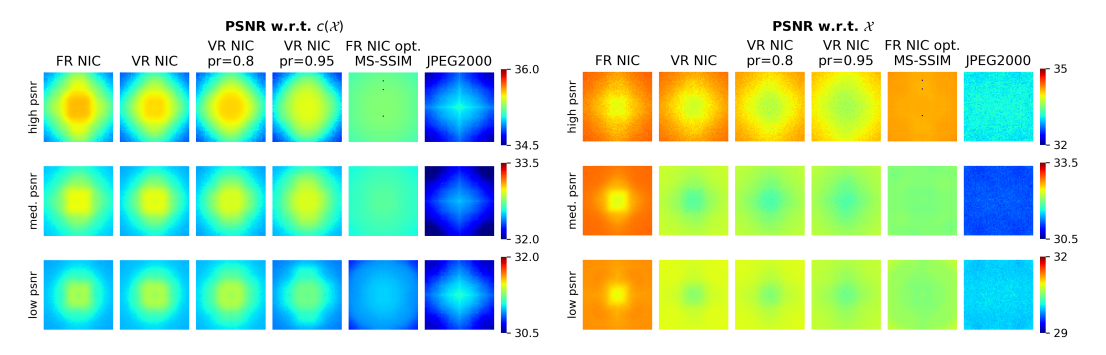


Figure 22: Fourier heatmap equivalent to Figure 6 under a fixed-PSNR constraint.

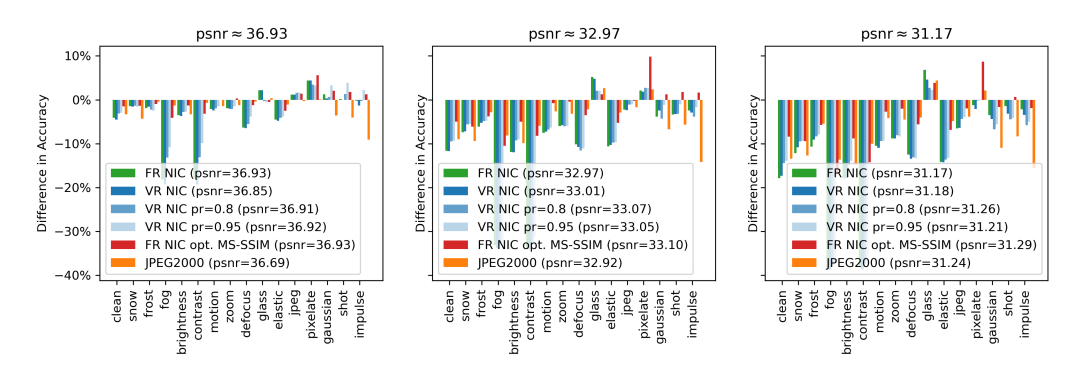


Figure 23: Difference in accuracy equivalent to Figure 9 under a fixed-PSNR constraint.

I Image compression methods

Here we provide details on the NIC methods considered in our analysis.

Fixed-Rate NIC. We use the hyperprior model $\mathcal C$ proposed by Ballé $\operatorname{\it et\,al.}$ as our base NIC model [9]. This model consists of an autoencoder that encodes the image X to latent space Y, quantizes Y to \hat{Y} and finally synthesizes $\mathcal C(X)$ from \hat{Y} . In practice, the quantized latent vector \hat{Y} is entropy encoded before transmission. Each of the components of the autoencoder has three convolutional layers, with the number of channels controlled by parameters N and M. Generalized divisive normalization (GDN) and inverse-GDNs are used as the non-linear activation functions in the autoencoder. GDNs implement local divisive normalization and have been shown to be particularly effective in image compression tasks [7, 8]. The model also has a hyperprior autoencoder with the exact same architecture as the other autoencoder, except with ReLU non-linearities. This encodes the prior on the entropy coding model and has been shown to improve performance. We based our implementation off of the one from [10].

Variable-Rate NIC. For our variable-rate NIC we implemented a model proposed by Dosovitskiy and Djolonga [17]. This model uses Loss Conditional Training (LCT) to train a variable-rate NIC based off the hyperprior model outlined in the previous paragraph. The model is trained over a continuous range of compression rates, optimizing the rate-distortion tradeoff at each. Once trained, this model can be adaptively used at any compression rate in the range, which makes it even more flexible than a discrete set of fixed-rate models. In order to condition the compression rate via LCT, all convolutional layers in the model are augmented with Feature-wise Linear Modulation (FiLM) layers [45]. In this case, these are small neural networks that take a conditioning parameter λ as input

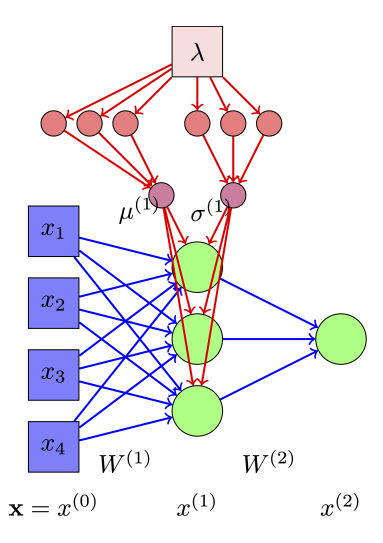


Figure 24: Cartoon of FiLM applied to a multi-layer perceptron. We consider pruning both the base layer weights (blue) and the film layer weights (red).

and output a μ and σ used to modulate the activations channel-wise based on the value of λ . More details on FiLM layers are provided in Appendix J

J Loss Conditional Training (LCT) model details

Suppose a layer in the CNN has activations f of size $W \times H \times C$. In Loss Conditional Training (LCT), these activations are augmented by μ and σ as follows,

$$\tilde{f} = \sigma f + \mu \tag{1}$$

where both μ and σ are vectors of size C.

Figure 24 shows a diagram of FiLM layers being applied to a small example network. Normally, without FiLM layers, the equation to calculate the features maps is

$$\mathbf{x}^{(1)} = \rho(W^{(1)}\mathbf{x}^{(0)} + \mathbf{b}^{(1)}),\tag{2}$$

where ρ is the activation function (e.g., ReLU). However, with FiLM layers, the weighted sum is first subject to augmentation with μ and σ . Thus, the new calculation is

$$\mathbf{x}^{(1)} = \rho(\boldsymbol{\sigma}^{(1)}(W^{(1)}\mathbf{x}^{(0)} + \mathbf{b}^{(1)})) + \boldsymbol{\mu}^{(1)}). \tag{3}$$

During training, a random λ is drawn with each mini-batch and used in two ways: 1) as input to the FiLM layers to modulate the feature maps and 2) in the mini-batch's loss function. During inference, the model takes as input a desired compression rate λ along with the input image. Notably, LCT and FiLM layers only affect the values of the activations (*i.e.*, feature maps), but not the *weights* on the convolutional layers or activation functions. This is an essential observation for applying pruning to a network with LCT.

K Gradual Magnitude Pruning (GMP)

To implement Gradual Magnitude Pruning (GMP), each layer is given binary mask of the same size as the original layer, which specifies which weights have been pruned (i.e., set to 0). Every Δt iterations, the mask is updated based on the magnitudes of the weights, such that the network has a desired sparsity. Suppose s_i is the initial sparsity (usually 0) at time t_0 and s_t is the target sparsity (0.8 or 0.95 in our case) which we want to reach after n steps, then the target sparsity at time step t is

$$s_t = s_f + (s_i - s_f) \left(1 - \frac{t - t_0}{n\Delta t} \right)^3$$
 (4)

for
$$t \in \{t_0, t_0 + \Delta t, \dots, t_0 + n\Delta t\}.$$
 (5)

The target sparsity equation is found to be especially effective because it causes weights to be pruned more quickly while the learning rate is still high and the weight-training on non-pruned weights can recover. After the desired sparsity is reached, the sparse network is trained for several more iterations. The pruning can be done layer-wise (*i.e.*, the mask must be updated such that each layer has the target sparsity) or globally (*i.e.*, the overall network must have the target sparsity, but the sparsities can differ between layers). Global pruning has been demonstrated to produce more performant sparse models than layerwise pruning, particularly at higher sparsity levels.

L Training setup and hyperparameters

Because the CLIC images are of varying size, we randomly crop them to size 256×256 during each epoch. We set N=M=192 for all NIC models. In the variable-rate models, we augment each convolutional layer with a FiLM layer which consists of two fully-connected layers and 128 hidden features. In all NIC experiments, the loss function is a weighted sum of a differentiable estimate of bpp and distortion. The distortion is mean squared error (MSE) for FR NIC, VR NIC, and VR NIC with pruning. In FR NIC opt. MS-SSIM the distortion is 1 - MS-SSIM. We train the fixed-rate and variable-rate models with mini-batches of size 8 for 5,000 and 10,000 epochs respectively (about 1 and 2 million mini-batch iterations). In the pruned models trained with GMP, we use global pruning between epochs 675 and 2400. The remaining epochs are used for tuning the sparse weights. Fixed-rate MSE models are trained over eight values of λ : {0.0012, 0.005, 0.01, 0.03, 0.05, 0.1, 0.15, and 0.26}. Variable-rate MSE models are trained by sampling λ from a log-uniform distribution over [0.0012, 0.26]. Fixed-rate MS-SSIM models are trained over several values of $\lambda \in [1, 1000]$.

M Mathematical details

M.1 Derivation of lemma 5.1

Let $\mathcal{X} \in \mathbb{R}^{N \times p}$ be a dataset (whose datapoints are the rows) with mean 0 and covariance $\Sigma = \frac{1}{N} \mathcal{X}^T \mathcal{X}$. Consider the problem of linearly auto-encoding \mathcal{X} with latent space \mathbb{R}^r , where $r \leq p$:

$$\min_{W_1 \in M(r,p), W_2 \in M(p,r)} \frac{1}{2} |\mathcal{X}W_1^T W_2^T - \mathcal{X}|^2.$$
 (6)

It is a theorem of Eckart and Young [18] that for any solution W_1, W_2 of eq. (6) the product $\mathcal{C} = W_2 W_1$ is an orthogonal projection onto the subspace spanned by the top r principal components of \mathcal{X} (see also [6] and for more recent developments and additional references, [46, 34]). Informally, this theorem says "linear autoencoders perform PCA." Formally, if $\mathcal{X} = USV^T$ is an SVD and V[:r] is the first r rows of V, then $W_2W_1 = V[:r]^TV[:r]$. It follows that the reconstruction error $\mathcal{L}(X)$ on a new input $X \in \mathbb{R}^p$ admits a simple closed form: let V_1, \ldots, V_p be the principal components of X (rows of V above), and write

$$X = \sum_{i} c_i V_i; \text{ then } \mathcal{L}(X) = \sum_{i>r} c_i^2.$$
 (7)

Suppose now that \mathcal{X} is a dataset of natural images. We will replace the single index i for $X=(X_1,\ldots,X_p)\in\mathbb{R}^p$ with 3 indices h,i,j for an image tensor $X=(X_{h,i,j})\in\mathbb{R}^{KHW}$ (here h is viewed as the channel index and i,j as the spatial indices); we will also commit mild abuse of notation by letting the matrices W_i act on flattened (vectorized) tensors. Let $F:\mathbb{R}^{KHW}\to\mathbb{R}^{KHW}$ denote the spatial discrete Fourier transform. We introduce the notation

$$\hat{\mathcal{X}} = \mathcal{X}F^T \text{ and } \hat{\mathcal{C}} = F\mathcal{C}F^T,$$
 (8)

and we will frequently use the shorthand "hat" decoration " $\hat{-}$ " to denote F as well, for ease of notation. Just as $\mathcal C$ projects onto the subspace spanned by the top r principal components of $\mathcal X$, $\hat{\mathcal C}$ projects onto the subspace spanned by the top r principal components of $\hat{\mathcal X}$.

It has long been known that when transformed to (spatial) Fourier frequency space, there are reasonable (coarse) descriptions of the statistical distribution of natural images. Its variances in

⁷although it is in general not the case that $W_1 = V[:r], W_2 = V[:r]^T$, see [46, §G] for discussion.

spatial frequencies (i, j) can be modelled as $\frac{1}{|i|^{\alpha} + |j|^{\beta}}$ where $\alpha, \beta \approx 2$ and its covariances drop off rapidly away from the diagonal [12, 1, 35]. These two facts motivate the following assumptions:

- (I) The principal components of $\hat{\mathcal{X}}$ are roughly aligned with the spatial Fourier frequency basis.
- (II) The associated variances are monotonically decreasing with frequency magnitude (more specifically according to the power law $\frac{1}{|i|^{\alpha}+|j|^{\beta}}$).

Assuming $\alpha = \beta = 2$, the above would suggest that $\hat{\mathcal{C}}$ projects a Fourier transformed image $\hat{X} = FX$ onto Fourier basis vectors corresponding to spatial frequencies (i,j) with $i^2 + j^2 \leq \frac{r}{\pi K}$. That is,

$$(\hat{\mathcal{C}}\hat{X})_{:,ij} \approx \begin{cases} \hat{X}_{:,ij} & \text{if } i^2 + j^2 \le \frac{r}{\pi K} \\ 0 & \text{otherwise.} \end{cases}$$
 (9)

where $\hat{X}_{:,ij}$ denotes the components of \hat{X} corresponding to spatial frequency (i,j) (this is a vector of dimension K, the number of channels in the image dataset). Together with the identity $F\mathcal{C}X = \hat{\mathcal{C}}\hat{X}$, eq. (9) yields lemma 5.1.

Below, we use the above analysis to get some qualitative insights into the robustness and generalization metrics \mathcal{R} and \mathcal{G} introduced in section 3. In what follows let $c: \mathbb{R}^{KHW} \to \mathbb{R}^{KHW}$ be a corruption transformation.

M.2 Derivations of corollaries 5.2 and 5.3

Robustness: here we are interested in PSD(X - C(c(X))), which is simply the coordinatewise absolute value of $\hat{X} - \widehat{C(c(X))}$. Using the fact that in our simple model C is linear, we can expand like

$$\hat{X} - \widehat{\mathcal{C}(c(X))} = \hat{X} - \widehat{\mathcal{C}(c(X))} = \hat{X} - \widehat{\mathcal{C}}(\hat{X}) + \widehat{\mathcal{C}}(\widehat{c(X)} - \hat{X})$$

$$\tag{10}$$

so that for any frequency (i, j)

$$\begin{split} |(\hat{X} - \widehat{\mathcal{C}(c(X)}))_{:,ij}|^2 &= |(\hat{X} - \widehat{\mathcal{C}}(\hat{X}))_{:,ij}|^2 + 2\overline{(\hat{X} - \widehat{\mathcal{C}}(\hat{X}))_{:,ij}}\widehat{\mathcal{C}}(\widehat{c(X)} - \hat{X})_{:,ij} \\ &+ |\widehat{\mathcal{C}}(\widehat{c(X)} - \hat{X})_{:,ij}|^2 \\ &\approx \begin{cases} |(\widehat{c(X)} - \hat{X})_{:,ij}|^2 & \text{when } i^2 + j^2 \leq \frac{r}{\pi C} \\ |\hat{X}_{:,ij}|^2. & \text{otherwise.} \end{cases} \end{split}$$
(11)

Taking square roots, we see that

$$PSD(X - \mathcal{C}(c(X)))_{:,ij} \approx \begin{cases} |\widehat{(c(X)} - \hat{X})_{:,ij}| & \text{when } i^2 + j^2 \le \frac{r}{\pi C} \\ |\hat{X}_{:,ij}| & \text{otherwise;} \end{cases}$$
(12)

averaging over the dataset \mathcal{X} gives corollary 5.2. In particular, the cross term $2(\hat{X}-\hat{\mathcal{C}}(\hat{X}))_{:,ij}\hat{\mathcal{C}}(\widehat{c(X)}-\hat{X})_{:,ij}$ is identically 0. This suggests that autoencoder compressors trained on natural images are less robust to corruptions with large amplitude in low frequencies (in the sense that $|(\widehat{c(X)}-\hat{X})_{:,ij}|^2$ is large for small values of ij).

Generalization: here we are interested in PSD(c(X) - C(c(X))), which is simply the coordinatewise absolute value of $\widehat{c(X)} - \widehat{C(c(X))}$. Again using the fact that in our simple model $\mathcal C$ is linear, we can expand like

$$\widehat{c(X)} - \widehat{C(c(X)}) = \widehat{X} + (\widehat{c(X)} - \widehat{X}) - \widehat{C}(\widehat{X} + (\widehat{c(X)} - \widehat{X}))
= (\widehat{X} - \widehat{C}(\widehat{X})) + ((\widehat{c(X)} - \widehat{X}) - \widehat{C}(\widehat{c(X)} - \widehat{X})).$$
(13)

 $^{^{8}}$ Here we assume that our Fourier transform F has the property that frequency (0,0) corresponds to constant images.

From this we obtain

$$\begin{split} &|(\widehat{c(X)} - \widehat{C(c(X))})_{:,ij}|^{2} \\ &= |(\hat{X} - \widehat{C}(\hat{X}))_{:,ij}|^{2} + 2\overline{(\hat{X} - \widehat{C}(\hat{X}))_{:,ij}} ((\widehat{c(X)} - \hat{X}) - \widehat{C}(\widehat{c(X)} - \hat{X}))_{:,ij} \\ &+ |(\widehat{c(X)} - \hat{X}) - \widehat{C}(\widehat{c(X)} - \hat{X}))_{:,ij}|^{2} \\ &\approx \begin{cases} 0 & \text{when } i^{2} + j^{2} \leq \frac{r}{\pi C} \\ |\hat{X}_{:,ij}|^{2} + 2\overline{\hat{X}_{:,ij}} (\widehat{c(X)} - \hat{X})_{:,ij} + |(\widehat{c(X)} - \hat{X})_{:,ij}|^{2} & \text{otherwise.} \end{cases} \end{split}$$

Taking square roots and relating back to power spectral density, this says

$$PSD(c(X) - C(c(X)))_{:,ij}$$

$$\approx \begin{cases} 0 & \text{when } i^2 + j^2 \leq \frac{r}{\pi C} \\ \sqrt{|\hat{X}_{:,ij}|^2 + 2\widehat{X}_{:,ij}} \widehat{(c(X)} - \hat{X})_{:,ij} + |\widehat{(c(X)} - \hat{X})_{:,ij}|^2} & \text{otherwise} \end{cases}$$

and averaging over the dataset $\underline{\mathcal{X}}$ gives corollary 5.3. Equation (14) is more involved than eq. (11) – in particular, the "cross term" $2\widehat{X}_{:,ij}(\widehat{c(X)}-\widehat{X})_{:,ij}$ is in general non-zero. However, there are many cases where at least an expectation over the data set $\widehat{\mathcal{X}}$ the term $2\widehat{X}_{:,ij}(\widehat{c(X)}-\widehat{X})_{:,ij}$ vanishes (for example, when c is additive noise, or more generally when $\widehat{c(X)}-\widehat{X}$ is statistically independent of \widehat{X} .). In such cases, we can see that autoencoder compressors trained on natural images generalize less successfully to corruptions with large amplitude in high frequencies.

M.3 Autoencoder reconstruction error and data density more generally

Our findings on *generalization* (both the experimental results and analysis with linear autoencoders) is closely related to the widely observed *inverse correlation* between autoencoder reconstruction error and probability density. We will take the recent [28] as a jumping-off point. However, it is worth noting that this observation (or at least something similar to it) has been around for some time, at least since [4], and forms the basis for widespread use of autoencoders in anomaly detection.

Formally, [28, Observation 2] states that:

(*) For an autoencoder $\mathcal C$ the reconstruction error $|\mathcal C(X)-X|_2$ is positively correlated with $\frac{1}{p(X)}$, the probability density of the input data at X.

If we assume this observation holds, then some of our experimental findings regarding generalization to corrupted data admit a simple explanation: as discussed above, the probability density of natural images is heavily concentrated along low (spatial) Fourier frequencies. Hence for a corruption c such that c(X)-X is concentrated in high frequencies, it is reasonable to suspect that p(c(X))< p(X), and given the assumed positive correlation of $\frac{1}{p(X)}$ with $|\mathcal{C}(X)-X|_2$, that

$$|\mathcal{C}(c(X)) - c(X)|_2 > |\mathcal{C}(X) - X|_2,$$
 (16)

i.e. the reconstruction error of the corrupted datapoint, related to our generalization metric, is higher than that of the clean datapoint X.

Remark M.1. In some sense, (*) is a simple consequence of learning via risk minimization. Let $\mathcal{C}: M \to M$ be an autoencoder on a manifold M with finite volume (for example, the image hypercube $[0,1]^{CHW}$). Let $\ell(\mathcal{C}(X),X)$ be a reconstruction loss on a point $X \in M$ and let p(X) be the probability density of input data on M, assumed to be positive everywhere (otherwise, discussing correlation with $\frac{1}{p(X)}$ is troublesome). The risk in this situation is

$$\mathcal{L}(\mathcal{C}) := \int_{M} \ell(\mathcal{C}(X), X) p(X) dx \tag{17}$$

Note that $\ell(\mathcal{C}(X), X)$ and $\frac{1}{p(X)}$ will be positively correlated provided that their covariance is positive. By definition this covariance is

$$\int_{M} \ell(\mathcal{C}(X), X) \frac{1}{p(X)} p(X) dx - \int_{M} \ell(\mathcal{C}(X), X) p(X) dx \cdot \int_{M} \frac{1}{p(X)} p(X) dx$$

$$= \int_{M} \ell(\mathcal{C}(X), X) dx - \mathcal{L}(\mathcal{C}) \cdot \text{vol} M. \tag{18}$$

Since at present we only care about the sign of the covariance, we can divide by volM to obtain

$$\int_{M} \ell(\mathcal{C}(X), X) \frac{dx}{\text{vol}M} - \mathcal{L}(\mathcal{C}); \tag{19}$$

the first term is the risk of \mathcal{C} with respect to the *uniform* distribution on M. In words, eq. (19) is positive whenever \mathcal{C} performs better on the distribution p(X) than the uniform distribution, and this outcome is to be expected for an autoencoder with sufficient capacity trained on a non-uniform distribution p(X).

Remark M.2. With notation as in the previous example, the result [3, Thm. 2] shows that the solution obtained with calculus of variations applied to an objective of the form

$$\min_{\mathcal{C}} \int_{M} \left(|\mathcal{C}(X) - X|_{2}^{2} + \sigma^{2} |\nabla_{X} \mathcal{C}(X)|_{2}^{2} \right) p(X) dx \tag{20}$$

(i.e. mean squared error loss and an ℓ^2 penalty on gradient norms) satisfies

$$C(X) - X = \sigma^2 \nabla_X \log p(X) + o(\sigma^2) \text{ and}$$
 (21)

$$\nabla_X \mathcal{C}(X) = I + \sigma^2 \operatorname{Hess}_X \log p(X) + o(\sigma^2) \text{ as } \sigma \to 0.$$
 (22)

In particular, the reconstruction error $|\mathcal{C}(X) - X|_2$ is proportional to the gradient norm $|\nabla_X \log p(X)|_2$ (up to higher order terms in σ^2 as $\sigma \to 0$). Since

$$|\nabla_X \log p(X)|_2 = \frac{1}{p(X)} |\nabla_X p(X)|_2,$$

this result sheds a more precise and quantitative light on (*).

Equation (22) may also shed some light on robustness of C as measured by R: indeed, if we assume c(X) - X is small,

$$C(c(X)) - X = C(X + c(X) - X) - X \approx C(X) + \nabla_X C^T(c(X) - X) - X. \tag{23}$$

Applying eqs. (21) and (22) gives the approximation

$$C(X) + \nabla_X C^T(c(X) - X) - X \approx \sigma^2 \nabla_X \log p(X) + (I + \sigma^2 \operatorname{Hess}_X \log p(X))(c(X) - X) + o(\sigma^2)$$
(24)

as $\sigma \to 0$. Taking norms squared we get

$$|\mathcal{C}(c(X)) - X|^2 \approx \sigma^2 |\nabla_X \log p(X)|^2$$

$$+ 2\sigma^2 \nabla_X \log p(X)^T (I + \sigma^2 \operatorname{Hess}_X \log p(X)) (c(X) - X)$$

$$+ |(I + \sigma^2 \operatorname{Hess}_X \log p(X)) (c(X) - X)|^2 + o(\sigma^2)$$
(25)

as $\sigma \to 0$. If we again make the simplifying assumption that c(X) - X is random and independent of X, then after taking the expectation over c (here denoted by E_c) we obtain

$$E_c[|\mathcal{C}(c(X)) - X|^2] \approx \sigma^2 |\nabla_X \log p(X)|^2 + E_c[|(I + \sigma^2 \operatorname{Hess}_X \log p(X))(c(X) - X)|^2] + o(\sigma^2)$$
(26)

as $\sigma \to 0$. If we let $\alpha_1 \ge \alpha_2 \ge \cdots \ge \alpha_p$ be the eigenvalues of $\operatorname{Hess}_X \log p(X)$ and choose σ small enough that $1 + \frac{\sigma^2}{\alpha_i} > 0$ for all i, we see that the norm

$$|(I + \sigma^2 \operatorname{Hess}_X \log p(X))(c(X) - X)|^2$$
(27)

surpresses (resp. magnifies) contributions from components of c(X)-X along the eigenvectors associated with α_i for large (resp. small) i. Note that it is reasonable as a first approximation to expect $\operatorname{Hess}_X \log p(X)$ to be negative definite (this is precisely the case when p is a Gaussian distribution, and more generally the requirements $p(X) \geq 0$ and $\int p(X)dX = 1$ put restrictions on the extent to which $\operatorname{Hess}_X \log p(X)$ can exhibit non-negative eigenvalues). In this case the large (resp. small) values of i correspond to the eigenvectors in directions of "sharpest" (resp. "shallowest") curvature of the graph of p(X). Explicitly, if X is Gaussian with covariance Σ , then $Hess_X \log p(X) = \Sigma^{-1}$, and if $\lambda_1 \geq \lambda_2 \geq \cdots \geq \lambda_p$ are the eigenvalues of Σ then $\alpha_i = -\frac{1}{\lambda_i}$ for all i. In this case we see that the norm in eq. (27) surpresses (resp. magnifies) contributions from components of c(X) - X along principal components with low (resp. high) variance. Note that this provides a takeaway qualitatively similar to that of corollary 5.2.

M.4 A fundamental robustness-generalization inequality

The similarity between the \mathcal{R} heatmaps for glass blur in fig. 4 and the PSDs of the corruptions themselves appearing in fig. 1a has a simple explanation in terms of a fundamental relationship between \mathcal{D}, \mathcal{G} and \mathcal{R} . One can show (via two applications of the triangle inequality) that

$$\frac{1}{N} \sum_{k=1}^{N} PSD(X_k - c(X_k)) - \mathcal{G}(\mathcal{C}, \mathcal{X}, c) \le \mathcal{R}(\mathcal{C}, \mathcal{X}, c) \le \frac{1}{N} \sum_{k=1}^{N} PSD(X_k - c(X_k)) + \mathcal{G}(\mathcal{C}, \mathcal{X}, c). \tag{28}$$

In the case of glass blur, generalization error is very low, so eq. (28) reduces to $\mathcal{R} \approx \frac{1}{N} \sum_{k=1}^{N} PSD(X_k - c(X_k))$, where the right-hand side is the average PSD of the corruption itself.

N Tables of classification accuracies

	No Compression
clean	0.76
snow	0.34
frost	0.31
fog	0.46
brightness	0.69
contrast	0.44
motion blur	0.37
zoom blur	0.35
defocus blur	0.36
glass blur	0.16
elastic transform	0.53
jpeg compression	0.59
pixelate	0.50
gaussian noise	0.32
shot noise	0.29
impulse noise	0.32

Table 1: Classification accuracies without compression on the validation split of ImageNet-C.

	FR NIC	VR NIC	VR NIC pr=0.8	VR NIC pr=0.95	FR NIC opt. MS-SSIM	JPEG2000
			bpp = 1.23			
clean	0.74	0.73	0.73	0.73	0.74	0.72
snow	0.33	0.33	0.33	0.32	0.32	0.30
frost	0.30	0.30	0.29	0.28	0.30	0.30
fog	0.36	0.36	0.36	0.36	0.41	0.45
brightness	0.67	0.67	0.66	0.66	0.67	0.65
contrast	0.36	0.35	0.34	0.36	0.40	0.44
motion blur	0.36	0.36	0.35	0.36	0.37	0.36
zoom blur	0.34	0.34	0.33	0.34	0.35	0.34
defocus blur	0.32	0.32	0.32	0.33	0.34	0.36
glass blur	0.17	0.17	0.16	0.16	0.16	0.17
elastic transform	0.50	0.50	0.49	0.49	0.50	0.52
jpeg compression	0.60	0.60	0.61	0.61	0.60	0.59
pixelate	0.53	0.53	0.54	0.54	0.58	0.51
gaussian noise	0.33	0.33	0.34	0.34	0.36	0.31
shot noise	0.34	0.33	0.33	0.33	0.32	0.28
impulse noise	0.32	0.31	0.32	0.34	0.35	0.23
			bpp = 0.77			
clean	0.72	0.71	0.71	0.71	0.71	0.69
snow	0.33	0.32	0.32	0.32	0.29	0.27
frost	0.29	0.29	0.28	0.28	0.27	0.29
fog	0.28	0.27	0.27	0.25	0.36	0.41
brightness	0.65	0.65	0.65	0.64	0.65	0.62
contrast	0.26	0.25	0.26	0.24	0.37	0.41
motion blur	0.35	0.35	0.34	0.34	0.36	0.35
zoom blur	0.33	0.33	0.32	0.32	0.35	0.33
defocus blur	0.30	0.29	0.29	0.29	0.33	0.35
glass blur	0.19	0.19	0.17	0.17	0.17	0.18
elastic transform	0.48	0.48	0.48	0.47	0.48	0.51
jpeg compression	0.60	0.60	0.60	0.60	0.59	0.58
pixelate	0.55	0.55	0.54	0.54	0.60	0.52
gaussian noise	0.33	0.32	0.32	0.34	0.34	0.31
shot noise	0.29	0.29	0.29	0.32	0.31	0.28
impulse noise	0.23	0.30	0.23	0.32	0.33	0.26
Impaise noise	0.01	0.50	bpp = 0.24			3.20
alaan	0.50	0.56		0.56	0.60	0.52
clean	0.58	0.56	0.58	0.56	0.60	0.52
snow	0.22	0.22	0.22	0.21	0.18	0.14
frost	0.20	0.20	0.20	0.20	0.20	0.19
fog	0.08	0.06	0.06	0.05	0.18	0.21
brightness	0.51	0.49	0.50	0.49	0.53	0.43
contrast	0.07	0.05	0.05	0.05	0.20	0.25
motion blur	0.27	0.25	0.26	0.25	0.30	0.29
zoom blur	0.26	0.25	0.26	0.25	0.29	0.27
defocus blur	0.24	0.22	0.22	0.21	0.27	0.28
glass blur	0.23	0.21	0.19	0.19	0.24	0.24
elastic transform	0.39	0.37	0.37	0.36	0.42	0.42
jpeg compression	0.52	0.51	0.52	0.51	0.53	0.47
pixelate	0.49	0.47	0.48	0.47	0.54	0.47
gaussian noise	0.28	0.28	0.25	0.25	0.27	0.27
shot noise	0.28	0.27	0.25	0.25	0.28	0.26
impulse noise	0.29	0.28	0.25	0.25	0.26	0.26

Table 2: Classification accuracies from Figure 9

	FR NIC	VR NIC	VR NIC pr=0.8	VR NIC pr=0.95	FR NIC opt. MS-SSIM	JPEG2000
			PSNR=36.93			
clean	0.72	0.71	0.73	0.73	0.74	0.72
snow	0.33	0.32	0.33	0.32	0.33	0.30
frost	0.29	0.29	0.29	0.28	0.30	0.30
fog	0.28	0.27	0.33	0.35	0.42	0.45
brightness	0.65	0.65	0.66	0.66	0.67	0.65
contrast	0.26	0.25	0.31	0.34	0.41	0.44
motion blur	0.35	0.35	0.35	0.36	0.37	0.36
zoom blur	0.33	0.33	0.33	0.34	0.35	0.34
defocus blur	0.30	0.29	0.30	0.32	0.35	0.36
glass blur	0.19	0.19	0.16	0.16	0.16	0.17
elastic transform	0.48	0.48	0.49	0.49	0.50	0.52
jpeg compression	0.60	0.60	0.61	0.47	0.60	0.52
pixelate	0.55	0.55	0.54	0.54	0.56	0.51
gaussian noise	0.33	0.32	0.33	0.35	0.34 0.31	0.28
shot noise	0.29	0.29	0.30	0.33		0.25
impulse noise	0.31	0.30	0.31	0.34	0.33	0.23
			PSNR=32.97			
clean	0.64	0.64	0.66	0.66	0.71	0.67
snow	0.27	0.27	0.28	0.29	0.28	0.25
frost	0.25	0.25	0.26	0.26	0.27	0.28
fog	0.13	0.12	0.13	0.14	0.35	0.38
brightness	0.57	0.57	0.59	0.60	0.64	0.59
contrast	0.11	0.10	0.12	0.13	0.36	0.38
motion blur	0.30	0.30	0.30	0.31	0.36	0.34
zoom blur	0.29	0.29	0.29	0.29	0.35	0.32
defocus blur	0.26	0.25	0.24	0.25	0.32	0.34
glass blur	0.22	0.21	0.18	0.19	0.18	0.19
elastic transform	0.42	0.43	0.43	0.43	0.48	0.50
jpeg compression	0.57	0.57	0.58	0.58	0.59	0.57
pixelate	0.53	0.52	0.53	0.53	0.60	0.53
gaussian noise	0.28	0.29	0.28	0.31	0.33	0.25
shot noise	0.26	0.26	0.26	0.28	0.31	0.23
impulse noise	0.29	0.29	0.28	0.30	0.33	0.17
			PSNR=31.17			
clean	0.58	0.58	0.61	0.62	0.67	0.62
snow	0.22	0.23	0.24	0.25	0.25	0.21
frost	0.20	0.22	0.22	0.23	0.25	0.25
fog	0.20	0.22	0.08	0.23	0.29	0.23
brightness	0.51	0.51	0.54	0.55	0.60	0.54
_						
contrast	0.07	0.06	0.07	0.08	0.30	0.34
motion blur	0.27	0.26	0.28	0.28	0.34	0.33
zoom blur	0.26	0.26	0.27	0.27	0.33	0.31
defocus blur	0.24	0.23	0.23	0.23	0.30	0.32
glass blur	0.23	0.21	0.19	0.19	0.20	0.21
elastic transform	0.39	0.39	0.39	0.40	0.46	0.48
jpeg compression	0.52	0.53	0.55	0.55	0.57	0.55
pixelate	0.49	0.48	0.50	0.50	0.59	0.53
gaussian noise	0.28	0.28	0.25	0.26	0.30	0.21
shot noise	0.28	0.26	0.25	0.25	0.30	0.21
impulse noise	0.29	0.28	0.26	0.27	0.30	0.16

Table 3: Classification accuracies from Figure 23